

**DESIGN OF A SMALL, AFFORDABLE LOW INTENSITY FOCUSED
ULTRASOUND DEVICE FOR VAGUS NERVE STIMULATION**

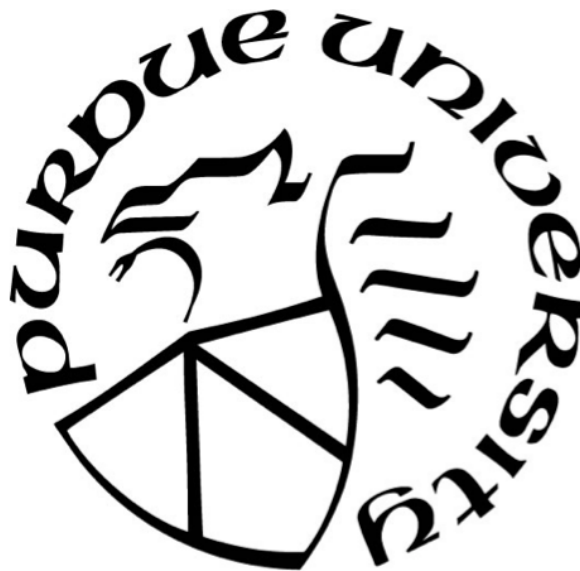
by
Kelsey C. Bayer

A Thesis

Submitted to the Faculty of Purdue University

In Partial Fulfillment of the Requirements for the degree of

Master of Science in Biomedical Engineering



Department of Biomedical Engineering

West Lafayette, Indiana

December 2017

THE PURDUE UNIVERSITY GRADUATE SCHOOL
STATEMENT OF THESIS APPROVAL

Dr. Pedro Irazoqui, Chair

Department of Biomedical Engineering

Dr. Craig Goergen

Department of Biomedical Engineering

Dr. Eduardo J. Juan García

Department of Electrical and Computer Engineering

Approved by:

Dr. George R. Wodicka

Head of the Departmental Graduate Program

ACKNOWLEDGEMENTS

I want to first thank all of my colleagues at the Center for Implantable Devices (CID) lab. Their constant support and strange brand of humor have made my time at Purdue as an undergraduate and as a graduate student enjoyable. I of course want to thank my professor Dr. Pedro Irazoqui for providing me with the opportunity to pursue a higher education. I also want to thank my other committee member, Dr. Craig Goergen, for always being available to give support, advice, and edits.

I received a lot of help along the way for this project, and I want to highlight the people that were critical to the development of this device. This project began with Dr. Eduardo Juan García lending us his focused ultrasound system. I want to thank his lab for their generosity and for his in depth focused ultrasound advice. I specifically want to thank one of his students, Christian J Colon Ortiz, for flying out to work on the matching network with me. For the amplification network, I need to thank Chris Quinkert, Jack Williams, and Jay Shah for always answering my electrical engineering questions and explaining difficult concepts to me. For the fabrication of my device, I need to thank Dan Pederson, Jesse Somann, and Kevin Buno for their help. From Paul Robinson's Lab I specifically want to thank Jennifer Sturgis and Kathy Ragheb for picking up our blood samples and processing them. From the statistical department, I want to thank Ahmad Hakeem Abdul Wahab for all of his help with the data analysis.

Last, but certainly not least, I need to thank the CID lab manager, Gabriel Albors, and my partner in crime, Kelsey Wasilczuk. They were instrumental to the project from the brainstorming stage all the way to the animal work. None of this would have been possible without their guidance and support. Kelsey's innovation, persistence, and attention to detail have been essential to the progression of the project. I could not have asked for a better partner to spend hours of research discussion and animal work with.

This project is for my family and friends for all of their love and support over the years.

TABLE OF CONTENTS

LIST OF TABLES	vi
LIST OF SUPPLEMENTARY TABLES	vii
LIST OF FIGURES	viii
LIST OF SUPPLEMENTARY FIGURES	x
ABBREVIATIONS	xi
ABSTRACT	xii
1. INTRODUCTION	1
1.1. The Role of the Inflammatory Response in Depression	1
1.2. The Effect of Vagus Nerve Stimulation on Cytokines	1
1.3. Focused Ultrasound Overview	2
1.3.1. Piezoceramic Characteristics	2
1.3.2. Beam Formation Methods	3
1.3.3. Matching and Backing Layers	3
1.3.4. Impedance Matching	4
1.3.5. Signal Amplification	6
1.4. Calculating Intensity	7
1.5. High Intensity Focused Ultrasound	8
1.6. Low Intensity Focused Ultrasound	8
1.7. Study Overview	9
2. METHODS	10
2.1. Transducer Design	10
2.1.1. Earlier Prototypes	10
2.1.2. PZT Selection	10
2.1.3. Transducer Geometry	12
2.1.4. Backing and Matching Layer	12
2.1.5. Matching Network	13
2.1.6. Power Amplifier	15
2.1.7. PCB Design	16
2.2. Bench Top Characterization	16

2.3.	Surgical Overview	17
2.3.1.	Surgical Setup	17
2.3.2.	Pre-Made LPS Procedure.....	17
2.3.3.	Surgical Timeline.....	18
2.3.4.	Flow Cytometry	19
2.3.5.	Surgical Considerations	19
2.4.	Statistical Analysis	19
3.	RESULTS.....	21
3.1.	Geometric Comparison	21
3.2.	Price Comparison	22
3.3.	Matching Network Development	23
3.4.	LIFU Device Characterization	25
3.5.	Animal Study.....	28
4.	DISCUSSION.....	30
4.1.	LIFU Design Goal Overview	30
4.2.	PZT Shape Considerations	31
4.3.	PZT Material Considerations	32
4.4.	Matching Network Considerations	33
4.5.	Prototyping Design Considerations.....	34
4.5.1.	Prototype I.....	34
4.5.2.	Prototype II	36
4.5.3.	Prototype III	38
4.6.	Size and Cost Considerations	38
4.7.	Intensity Considerations	39
4.8.	Surgical and Statistical Considerations	40
4.8.1.	Animal Exclusion Criteria	40
4.8.2.	Analysis of TNF- α Concentration.....	41
4.8.3.	Studentized Residuals	42
4.9.	Future Considerations	44
5.	CONCLUSIONS	45
	REFERENCES	46
	SUPPLEMENTARY INFORMATION	52

LIST OF TABLES

Table 1: PZT Material Properties Comparison	10
Table 2: LIFU Transducer Dimensions	12
Table 3: Potential combinations of inductors and capacitors for matching L network	14
Table 4: 50 Ohm Application Circuit Values for 450 kHz	15
Table 5: Bill of Materials for H-115 System	22
Table 6: Bill of Materials for LIFU Device	23
Table 7: PZT Impedance Characterization	23
Table 8: All potential inductor and capacitor values for series X_m component and shunt B_m component	24
Table 9: Final shunt inductor and series capacitor values for case 2 combination of series X_c and shunt B_m components and the calculated power delivered.....	24
Table 10: A meaningful difference between the Cohen's h proportions can be deemed small (greater than 0.2), medium (greater than 0.5) or large (greater than 0.8).....	28

LIST OF SUPPLEMENTARY TABLES

Table S1: Calculated values for matching network efficiency	52
Table S2: SAS 94 generated studentized residual data for the FUS and control rats at the time point “90 minutes.” The data FUSx005 has the largest residual studentized value and is above +2.0.	53
Table S3: SAS 94 generated studentized residual data for the kept FUS and control rats at the time point “90 minutes.” The data for FUSx009 has the largest residual studentized value and is above +2.0.	53
Table S4: Matching Network Components.....	57
Table S5: Amplification Network Components	57
Table S6: Measured V_{pp} values for Prototype I without and with epoxy layer of arbitrary thickness	57
Table S7: Measured impedance values for one PZT element with wires upon arrival, immediately after being incorporated into transducer, and one week after being incorporated into transducer	58

LIST OF FIGURES

Figure 1: Shape of FUS beam	3
Figure 2: (a) Van Dyke's Model at Resonance (b) Equivalent Circuit Representation of a PZT ..	5
Figure 3: FOCUS generated simulations. (a) Geometry for phased array. (b) Normalized intensity field based on phased array geometry. (c) Normalized intensity along the z axis to simulate the location of the focal region from the center of the transducer. The depth of the transducer was modeled to be 4 mm.	11
Figure 4: SolidWorks design of transducer geometry. Scale bar = 5 mm.	12
Figure 5: Setup for applying a specific matching layer thickness to transducer	13
Figure 6: Cross-sectional view demonstrating even application of matching layer	13
Figure 7: Matching L Networks for eight potential combinations of inductors and capacitors. (a) Network used when impedance of transducer is less than impedance of source. (b) Network used when impedance of transducer is greater than impedance of source.	14
Figure 8: 50 Ohm Application Circuit Schematic for 450 kHz	15
Figure 9: Bench top test setup for measuring the amplitude of the soundwaves with a hydrophone. The hydrophone was secured in place and the LIFU device was moved in the x and z axis using a stereotactic frame.	17
Figure 10: Surgical Timeline	18
Figure 11: Surgical setup of rat with LIFU device positioned over the vagus nerve and a left leg catheter for blood collection.	19
Figure 12: (a) Final LIFU Device Design. (b) Amplification network with heatsink over nine amplifiers. (c) Final dimensions of 50 mm x 57 mm x 76 mm.	21
Figure 13: System comparison of H-115 and LIFU device: transducer, matching network, and amplification network. The six inch ruler was included for reference.	22
Figure 14: Graphical representation of ideal vs actual components selected for matching network	25
Figure 15: 2D intensity map of the LIFU device at -3 dBm. The focal region was 1 mm x 4 mm and occurred between 10 mm and 12 mm from the center of the transducer. The color bar represents the intensity in W/cm^2	26

Figure 16: 2D intensity map of the LIFU device at -3 dBm. The focal region was shifted 8 mm from the center of the transducer. The focal region was 1 mm x 1 mm and occurred between 10 mm and 14 mm from the center of the transducer. The color bar represents the intensity in W/cm^2 .	26
Figure 17: A focal region of 4 mm x 2 mm was evaluated 10 mm to 12 mm from the center of the transducer. At this position the amplitude was varied from - 6 dBm to 9 dBm. The focal region shape and location varied based on the amplitude. The color bar represents the intensity in W/cm^2 .	27
Figure 18: TNF- α average concentration data for 8 rats that received therapy from the LIFU device and 5 rats that did not receive therapy. Based on events recorded in the surgical logs, 4 of the FUS rats were removed from the study.	28
Figure 19: Cohen's h proportional analysis of the three cytokines TNF- α , IL-6, and IL-10.	29
Figure 20: Evaluation of therapies at time point "90 minutes" for controls and the LIFU device. There was an n = 5 for control data. Error bar for the control represents standard deviation. Each FUS label represents one rat. There are no error bars for the FUS data because the data is represented as the average of two replicates.	29
Figure 21: H-115 Transducer with coupling cone mounted and positioned over the vagus.	31
Figure 22: H-115 Transducer, Coupling Cone, and Matching Network	31
Figure 23: Front and back of PZT element showing wires attached by the company	34
Figure 24: Prototype I. (a) Design of transducer without protective epoxy layer. (b) Finished prototype with protective epoxy layer and matching network.	35
Figure 25: Prototype II and Dremel job	37
Figure 26: Mold Putty Negatives	38

LIST OF SUPPLEMENTARY FIGURES

Figure S1: SAS 94 generated figures based on data. (a) P value of 0.0845. (b) The fit diagnostics.	54
Figure S2: SAS 94 generated figures based on data with removed FUSx005. (a) P value of 0.0274. (b) The fit diagnostics.....	55
Figure S3: SAS 94 generated figures based on data with removed FUSx005, and FUSx009. (a) P value of 0.0062. (b) The fit diagnostics show a normal distribution and constant variance. These plots support that the assumptions and inferences are valid.	56

ABBREVIATIONS

Acoustic Instantaneous Intensity (I)
Capacitors (C)
Center for Implantable Devices (CID)
Focused Ultrasound (FUS)
High Intensity Focused Ultrasound (HIFU)
Inductors (L)
Interleukin 10 (IL-10)
Interleukin 6 (IL-6)
Intraperitoneal (IP)
Ketamine-Xylazine (ket/xyl)
Lead Zirconate Titanate (PZT)
Lipopolysaccharides (LPS)
Low Intensity Focused Ultrasound (LIFU)
Polyvinylidene Difluoride (PVDF)
Radio Frequency (RF)
Reflection Coefficient (Γ)
Resistors (R)
Selective Serotonin Reuptake Inhibitors (SSRIs)
Spatial Peak Pulse Average Intensity (I_{SPPA})
Spatial Peak Temporal Average Intensity (I_{SPTA})
Standing Wave Ratio (SWR)
Surface-Mount Device (SMD)
Treatment-Resistant Depression (TRD)
Tumor Necrosis Factor (TNF)
Vagus Nerve Stimulation (VNS)

ABSTRACT

Author: Bayer, Kelsey, C. MSBME

Institution: Purdue University

Degree Received: December 2017

Title: Design of a small, affordable low intensity focused ultrasound device for vagus nerve stimulation

Major Professor: Pedro Irazoqui

Depression is a serious public health issue that affects more than 300 million people worldwide. While there are antidepressant drugs to alleviate depressive symptoms, 10 – 30% of patients either do not respond or develop a tolerance to these drugs. Researchers have found a correlation between the inflammatory response and treatment-resistant depression (TRD). Blocking this inflammatory pathway with electrical vagus nerve stimulation (VNS) can reduce cytokine levels and depressive symptoms. However, placing an electrical VNS device is invasive, costly, and poses a risk to the vagus nerve. Low intensity focused ultrasound (LIFU) is a novel therapy that is able to both excite and suppress neuronal activity in neurological disorders. However, progression of this research area has been impeded by the size and price of these devices. I designed a 50 x 57 x 76 mm LIFU device that consists of a transducer, matching network, and amplification network. Next, I characterized my LIFU device with 2D intensity maps of the focused ultrasound (FUS) field. My device produced an instantaneous intensity up to 350 mW/cm². My colleagues and I applied the LIFU device on Sprague-Dawley rats (n=12) for VNS with the primary goal of reducing the inflammatory response. Five out of the eight rats that we analyzed showed a decrease in the cytokine TNF- α . Future work will involve design improvements and more animal studies with varying stimulation parameters. As FUS technology becomes smaller we move closer to wearable devices. As FUS technology becomes more affordable more research groups will have the opportunity to employ this novel therapy to investigate the pathophysiology of neurological disorders.

1. INTRODUCTION

1.1. The Role of the Inflammatory Response in Depression

Depression is a serious public health issue that affects more than 300 million people worldwide [1]. This disorder can have a debilitating effect on a person's everyday life and can lead to suicide. Around 800,000 people commit suicide every year with this being the second leading cause of death in 15 to 29 year olds [1]. In 2010, approximately \$210.5 billion dollars was spent directly and indirectly on depression. The categorical break down for this staggering number is based on work-place productivity, healthcare, and suicide related costs [2]. To better understand depression it is important to look into the pathophysiology. The monoamine hypothesis poses that depressive symptoms are the result of a deficiency in neurotransmitters such as serotonin, norepinephrine, and/or dopamine [3]–[5]. Antidepressant drugs, such as selective serotonin reuptake inhibitors (SSRIs), make more neurotransmitters available by blocking the reabsorption of neurotransmitters to alleviate depressive symptoms [6]. However, people using SSRIs can develop a tolerance to them over time and may not respond to other medications [7]–[10]. Treatment-resistant depression (TRD) is classified as a failure to respond to at least two trials of pharmaceutical drugs [11]. An estimated 50 – 60% of patients do not fully respond to antidepressant drugs, and of those 10 – 30% suffers from TRD [11]–[13]. Alternatively, new studies have found a correlation between the inflammatory response and TRD [7] [14]–[18]. As such, a promising method for treating major depressive disorder is to block the inflammatory signaling pathway by modulating cytokine levels [7], [19], [20].

1.2. The Effect of Vagus Nerve Stimulation on Cytokines

Studies are now focusing on the role of pro-inflammatory and anti-inflammatory cytokines in the inflammation response. Cytokines are a substance secreted by cells associated with the inflammatory system that communicate with the brain through neural and humoral pathways [21]. An increased expression of pro-inflammatory cytokines interleukin 6 (IL-6) and tumor necrosis factor (TNF- α) have been linked to patients with major depressive disorder and found in post-mortem brain samples of suicide victims [4], [7], [22]–[25]. Inflammation begins with the autonomic system, controlling key immune organs, such as the spleen, adrenal glands, and bone marrow [26]–[28]. The spleen is made up of mostly red pulp that filters and recycles blood components. There is also a small region of white pulp associated with the immune system that generates antigen-specific antibodies and produces and stores lymphocytes [29]. The inflammation response can be triggered by the presence of endotoxins. Endotoxins, also called lipopolysaccharides (LPS), are components of the outer membrane of Gram-negative bacteria [30]. LPS will react with LPS-sensitive cells mediating endotoxemia [26], [30], [31]. The resulting monocyte and macrophage production of TNF- α and other cytokines in the spleen can be blocked by stimulating the vagus nerve [31], [32]. The vagus nerve is composed of 20%

efferent and 80% afferent fibers and is often called the “wandering” nerve because of its vast distribution throughout the body as it travels from the brainstem to the abdomen. Vagus nerve stimulation (VNS) involves applying a mechanical or electrical signal to the nerve. Through the vagus nerve, indirect connections can be made to autonomic functions as well as brain regions associated with neuropsychiatric disorders [7]. Disease severity associated with inflammatory syndromes can be reduced through VNS and the subsequent regulation of cytokine production [21], [31]–[36].

In 1997 the U.S. FDA approved an implantable electrical VNS device for the treatment of refractory epilepsy [37]. A cuff is secured around the vagus nerve through which these implanted devices are able deliver electrical stimulation. Interestingly, there has been a reported decrease in depressive symptoms, even when epilepsy symptoms have not improved [37]. This phenomenon has been further explored in animal models specific to depression [37]. However, potential side effects of this therapy are voice alteration, cough, dyspnea, dysphagia, and neck pain or paresthesia. Also, efferent fiber damage due to cuffing was indicated by a decrease in Fluorogold transport in the rat model for chronic VNS studies [38]. Cuffing the nerve is an invasive and potentially damaging method. A solution to stimulate the nerve without cuffing it is focused ultrasound (FUS).

1.3. Focused Ultrasound Overview

1.3.1. Piezoceramic Characteristics

The noninvasive aspect of the sound waves produced by FUS technology has a wide range of medical and industrial applications. Ultrasound is classified as sound waves with a frequency above the human hearing limit of 20 kHz. Ultrasound is produced by a piezoelectric material when it is under some form of strain, such as mechanical or electrical. Inside the crystal structure of this material the ionic charge distribution is symmetric, but when external stress is applied there is a displacement of ionic charges and an overall net polarization [39]. If a voltage is the external stress, the material will resonate and convert electricity to sound waves [40]. In the 1940s research and commercialization of this piezoceramic material took off due to the discovery of barium titanate and lead zirconate titanate (PZT) [39]. The applications for this material expanded because of their increased dielectric and piezoelectric properties, and the introduction of dopants to further modify the piezoelectric properties. The fabrication process for PZTs begins with the powder preparation of lead oxide, titanium oxide, and zirconium oxide as the main components. This is followed by calcining, sintering, and machining. The final steps involve applying electrodes using a DC field to polarize the material giving it its piezoelectric qualities [39]. Today PZTs are the most popular type of piezoelectric material and are available in a variety of shapes with specific application-based properties.

1.3.2. Beam Formation Methods

FUS devices take advantage of the PZTs by inducing and directing sound waves to a specific location. The beam is made up of the Fresnel Zone (near field), Fraunhofer Zone (far field), and the focal point or region as seen in Figure 1 [41], [42]. Near-field diffraction occurs at a finite distance from the transducer and the scattered waves will influence the shape and size of the focal region. Far-field diffraction is not dependent on the distance between it and the transducer and the scattered waves begin to turn into planar waves [43],[44]. The benefit of this transducer technology is that the desired effect occurs in the focal region. Focusing of the beam can be achieved with a curved PZT element, a phased array, a lens, or by electronic method [40], [45]–[47]. Monolithic shapes such as hemispheres and spherical caps are a simple choice to generating a stable focused beam [48]. A phased array incorporates multiple PZT elements that can be geometrically and/or electronically focused. To electronically focus a phased array, time delays are applied to create strategic constructive and destructive waves to control the location of the focal region [49]. Each design has tradeoffs based on size, availability, and cost.

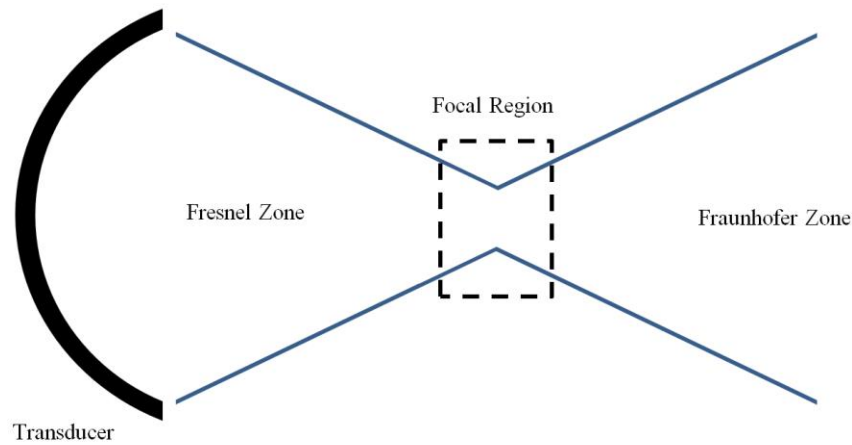


Figure 1: Shape of FUS beam

1.3.3. Matching and Backing Layers

To protect and enhance the design of a FUS device, a front and back layer can be applied to the PZT elements. The front layer is often referred to as a matching layer because, based on the thickness and properties of that matching layer material, the acoustic performance can be improved. To ensure maximum power transfer to the focal region studies have reported a quarter-wave thickness and the need for a specific impedance for the matching layer [49]–[52]. The impedance of the matching layer needs to be the square root of the product of the acoustic impedance of the transducer (Z_1) and the acoustic impedance of the medium (Z_2) the ultrasound will be traveling into [50],[53].

$$\text{Matching Layer Thickness} = \frac{\lambda}{4} \quad (1)$$

$$\text{Matching Layer Impedance} = \sqrt{Z_1 * Z_2} \quad (2)$$

In a phased array, cross-talk between elements can result in unwanted ringing leading to a reduction in acoustic power efficiency [49], [54]. Cross-talk is especially an issue in the case of phase shifting because the ability to control beamforming is compromised. It is important to maintain mechanical isolation between elements to avoid unwanted ringing. Options for fillings between elements are a variety of epoxy or silicone materials [52], [54]. The backing layer also plays an important role in acoustic performance. To avoid backward propagating waves from the back face of a PZT element, a silicone substrate can be applied as a backing layer to attenuate unwanted acoustic reverberations [49], [50], [52], [55]. Choosing a backing material with a high acoustic impedance will extend the waveform duration resulting in the absorption of unwanted signals, increased sensitivity, and increased signal amplitude [42], [50], [52], [55], [56]. It is also important to note that the addition of silicone and epoxy to a mechanically sensitive material will introduce capacitance into the system. The combination of the PZT elements, backing layer, and matching layer are referred to as the transducer.

1.3.4. Impedance Matching

To achieve maximum power transfer efficiency, the impedance of each element in the transducer needs to be matched to the source. If the source and transducer have mismatched impedances, then there will be a drastic decrease in the overall performance of the transducer [57]. A common impedance for matching in electronics is the standard transmission line impedance of 50Ω [51]. Most PZTs will have a resonance frequency in a narrow bandwidth where the amplitude of the sound waves will be the largest [58]. It is in this frequency range that impedance measurements must first be taken. Subsequently, these measurements are used to develop a network of reactive components for matching the transducer and the source. Reactive components are inductors (L) and capacitors (C). The IEEE Standard on Piezoelectricity recommends employing Van Dyke's Model as the equivalent circuit of a PZT [39], [57], [59]. Using the measured impedance values the mechanical behavior and electrostatic capacitance can be represented with a series RLC and parallel C in Figure 2a. The dielectric loss is negligible and not shown in the model [57]. L_s and C_s represent the resonance performance of the transducer. R_s is defined as the radiation and mechanical losses and C_o as the equivalent capacitance. However, if the mechanical losses are assumed to be relatively small, R_s can then represent the acoustic power emitted and be simplified to be in parallel or in series with C_o [57], [60]. Above the resonance frequency, specifically between the resonance frequency and the anti-resonance frequency, the equivalent circuit of the PZT is inductive. Below the resonance

frequency region, the equivalent circuit of the PZT is capacitive [39]. A simplified model of the equivalent circuit for a PZT element is shown in Figure 2b.

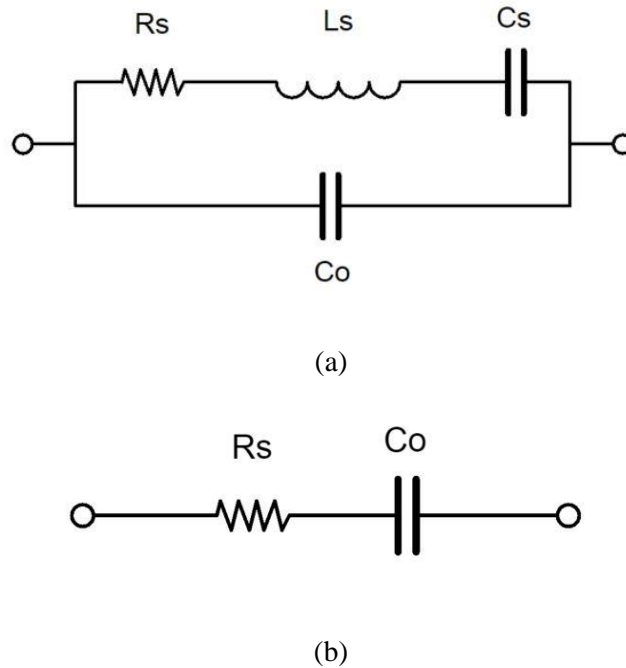


Figure 2: (a) Van Dyke's Model at Resonance (b) Equivalent Circuit Representation of a PZT

Parameters to consider when designing a matching network are the cost of components, size of components, and availability of specific values. When the frequency range is narrow and the number of components needs to be conservative, a combination of inductors and capacitors can be chosen to create a simple matching network [51], [57]. These reactive components will compensate for any capacitive effects within the transducer by matching the imaginary and real part of the complex conjugate of the transducer to the source [57]. Depending on which component is in series or in parallel with the transducer, the configuration can also act as a low or high pass filter. Both are acceptable designs, but the benefit of a low pass filter is that potential harmonics from the driving source will not affect the transducer [57]. Without a matching network the power transfer efficiency will be lost [58].

To evaluate the matching network, the standing wave ratio (SWR) and reflection coefficient (Γ) need to be calculated for. Standing waves are the result of a mismatch in impedance values between the load and the source. The result is that power is not efficiently delivered to the load and is instead lost when it is reflected back toward the source. A Γ of 0 and an SWR of 1 represents no reflection occurring in the system. To further characterize the effect of impedance mismatching the power reflected and delivered can be calculated for using the SWR and Γ [61][62].

$$SWR = \frac{Z_L}{Z_0} \quad (3)$$

$$\Gamma = \frac{SWR - 1}{SWR + 1} \quad (4)$$

$$Return Loss (dB) = -20 * \log_{10}(|\Gamma|) \quad (5)$$

$$Reflection Loss (dB) = -10 * \log_{10}(1 - \Gamma^2) \quad (6)$$

$$Power Reflected (\%) = |\Gamma|^2 * 100 \quad (7)$$

$$Power Delivered (\%) = (1 - |\Gamma|^2) * 100 \quad (8)$$

1.3.5. Signal Amplification

Another electrical block that needs careful design considerations within a FUS device is the amplification of the signal. The amplifier or network of amplifiers will receive a signal, amplify it, and pass it along to the matching network onto the transducer to create ultrasound. To avoid wasting energy in the form of heat dissipation, the amplifier needs to operate at a high efficiency. This is especially true when dealing with phased arrays where each PZT element will have its own matching and amplifying network. If the amplification network fails, depending on the type of amplifier, there is a risk of uncontrolled electrical power being applied to the transducer. Too much power can result in losing control of the ultrasound beam as well as damaging the PZT elements [63]. Damage to the PZT elements, such as overheating, could change their impedance [39], [63], [64]. A change in impedance will compromise the tuned matching network, which will result in inefficient power transfer.

Considerations for amplifier choice are power consumption, cost, size, and external components. When designing an amplification network, there are a variety of amplifiers to choose from such as power, operational, voltage, or current amplifiers. Power amplifiers have their input and output internally matched at 50 ohms, which is useful when operating between a 50 ohm source and a 50 ohm matched network for the transducer. Operational amplifiers have low efficiency and will consume power even in the absence of a signal. Voltage and current amplifiers are characterized by a mismatched input and output impedance of high or low to maximize voltage or current transfer [63]. Most of these will have a recommended application circuit for incorporating the part into the circuit design. The circuits consist of reactive components based on desired frequency range and impedance. These external networks are important to investigate before purchasing an amplifier when space conservation is a priority. Another option is to purchase an industrial sized amplifier that will have a controllable power output and guaranteed circuit protection guards. There are also amplifiers available for phased arrays that have two to sixty-one channels to independently drive each PZT element (E&I).

However, this option is not always feasible because these types of amplifiers can cost thousands of dollars.

1.4. Calculating Intensity

Evaluating the efficacy of a FUS device can be done with a hydrophone. A hydrophone is an instrument that contains a small PZT element that is sensitive to variations in pressure amplitude and will produce a proportional voltage. The PZT element is housed in a protective casing and is coupled to external conductors [65]. The hydrophone casing can be made of polyvinylidene difluoride (PVDF) which is a flexible and heat resistant material that is commonly used as electrical insulation. As the hydrophone records the pressure changes based on location from the transducer, the signal will pass through a voltage preamplifier. This is used to filter and/or add gain to the signal before it is displayed on an oscilloscope. Measurements are best taken in degassed and distilled water inside an anechoic like container that will not allow sound waves to reverberate off the walls and compromise the recorded values. This is a common method of characterization of the acoustic field for FUS devices. The recorded voltage amplitude and acoustic impedance of the medium can be used to calculate the acoustic instantaneous intensity (I), the rate at which sound energy flows through a unit area [40]. In the field of medical ultrasound, intensity is represented using W/cm^2 [66]. When the signal is pulsed, the type of intensity being reported can be specified (Equations 9 – 13). The acoustic intensity can further be defined as the spatial peak temporal average intensity (I_{SPTA}) and as the spatial peak pulse average intensity (I_{SPPA}). I_{SPTA} is the average intensity of a pulse repetition period and I_{SPPA} is the average intensity of a beam over a pulse duration [43], [65].

$$P = \frac{\left(\frac{V_{pp}}{gain} \right)}{OVC} \quad (9)$$

$$P_{rms} = \frac{P}{2\sqrt{2}} \quad (10)$$

$$I = \frac{P_{rms}^2}{Z} \quad (11)$$

$$I_{SPTA} = I * DC \quad (12)$$

$$I_{SPPA} = I_{SPTA} * PRP \quad (13)$$

Where V_{pp} is the recorded amplitude from the oscilloscope, P is the pressure amplitude (Pa), gain is set on the voltage preamplifier (dB), OVC is the hydrophone sensitivity (V/Pa), P_{rms} is the pressure amplitude (Pa), Z is the acoustic impedance of the medium (kg/ms^2), DC is the duty cycle (ms), and PRP is the pulse repetition period (s) [43], [65], [67].

1.5. High Intensity Focused Ultrasound

FUS devices can fall into the low intensity focused ultrasound (LIFU) or the high intensity focused ultrasound (HIFU) category. HIFU uses intensities of up to 100 W/cm^2 and is used for more extreme types of therapy such as, ablation, cavitation, and penetrating the blood brain barrier [68],[69]. The first FUS device to be FDA cleared was the Sonablate for ablation of prostate tissue in 2015. This device is used to non-invasively target compromised tissue and heat it up to 100°C with bursts of energy that cause thermal tissue coagulation, necrosis, cavitation, and heat shock [70]–[72]. The challenge associated with this type of technology is delivering therapy to the focal region without damaging the surrounding tissues [45]. The risk of unwanted energy absorption to the surrounding tissue is an issue for HIFU because ultrasound will attenuate faster at higher frequencies than at lower frequencies [41], [42]. With strides made in medical imaging technology, HIFU has become more clinically relevant because the therapy can be accurately positioned and the progress of tissue destruction monitored [70]. This type of therapy requires a substantial amount of power and precision. As PZT elements get smaller and more numerous in a phased array, the beam steering capability improves. It is common for HIFU devices to have anywhere from 16 to 256 elements [42], [73]–[78]. The tradeoff is that each of the active elements will need their own network for matching, amplification, and phase shifting. The typical input electrical power to each active element can range from 0.5 W to 6 W [51], [74], [75], [77]–[79]. Further, the PZT elements and electrical components will need to be of high quality to handle the power necessary for HIFU applications. All of these considerations quickly drive up the cost, size, and power consumption for these devices.

1.6. Low Intensity Focused Ultrasound

LIFU is often used for neuromodulation through mechanical stimulation. LIFU is commonly used in studies that focus on neurological or psychiatric disorders due to its ability to both excite and suppress neuronal activity [68], [80]–[85]. LIFU devices tend to employ concave shaped PZT elements and deliver a pulsed stimulation with an I_{SPTA} of up to 10 W/cm^2 [86]. Specifically, for neuromodulation studies an I_{SPTA} of less than 500 mW/cm^2 is used [68], [87],[88]. These lower intensity values are within compliance of the FDA limit for diagnostic imaging at an I_{SPTA} less than 700 mW/cm^2 [89],[90]. There are a number of studies that investigate the therapeutic effect of applying neuromodulation using intensities values in the mW/cm^2 range, however the parameters will vary greatly between studies [68], [87], [89]–[93]. The result of the LIFU therapy can also vary between excitatory or inhibitory based on the stimulation parameters. The benefit of the reversible biological effect of LIFU is that it can be used for modulation in a region of interest multiple times over an extended period of time without permanent tissue damage [68], [94]. The bimodal advantage of LIFU also yields challenges. A specific intensity may yield a wanted suppressive effect. However, just below or above that target intensity there will be a report of no effect or an excitatory effect, respectively [90], [95]. LIFU requires more fine tuning of parameters to achieve the desired neuromodulation outcome than HIFU, but the research is promising and worth continued exploration.

1.7. Study Overview

The Center for Implantable Devices (CID) at Purdue University is combining its expertise in biomedical and electrical engineering to look into the pathophysiology of the inflammatory response that has been linked to depression. The two forms of VNS therapy that CID is researching are electrical and LIFU. Through a collaboration formed between Dr. Pedro Irazoqui's CID lab and Dr. Eduardo J. Juan García's lab at the University of Puerto Rico - Mayagüez, resources were made available to create a team to look exclusively into LIFU. Using the H-115 Sonic Concepts FUS system loaned from Dr. Juan García's lab, my colleague, Kelsey Wasilczuk and I conducted research to investigate the merit of LIFU for the modulation of cytokines, specifically TNF- α . As this project continues to collect data on LIFU in VNS, I shifted my focus to building a device based on issues that arose in our research. As we began to look into purchasing our own device and accessory equipment for the CID lab we were unable to identify a system that was affordable. Many FUS transducers and the required backend electronics are expensive, large, and cumbersome. I address this issue by combining affordable off the shelf components. I will go into detail on the design decisions and construction of my transducer and circuit board consisting of matching and amplification networks. I then worked with Wasilczuk to conduct animal studies using my LIFU device. My research goal was to design a small, affordable LIFU device that could be used for cytokine modulation to relieve depressive symptoms.

2. METHODS

2.1. Transducer Design

2.1.1. Earlier Prototypes

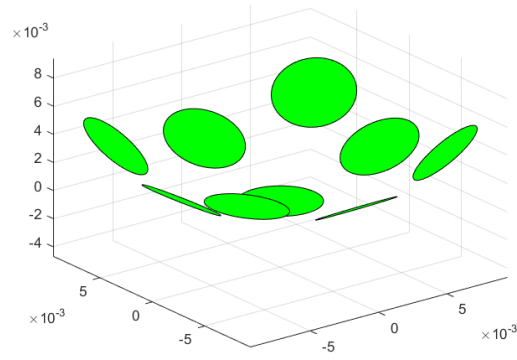
I constructed two prototypes before the final LIFU device. With each prototype of the device I was able to fine-tune the fabrication process and the electrical circuitry. A description of the prototyping process and how I arrived at my final design can be found in the discussion section. The results associated with these prototypes can be found in the supplementary section.

2.1.2. PZT Selection

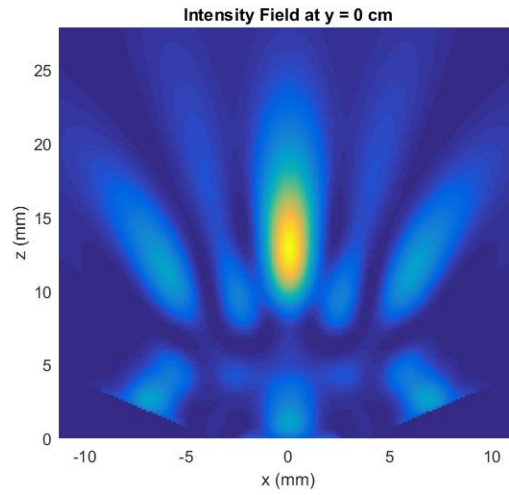
After correspondences with multiple PZT manufactures about price and availability of a single concave PZT element, I chose to instead build a phased array device because the materials would be more affordable. I purchased piezoceramic discs from STEMiNC. The dimensions of the PZTs were 5.0 mm diameter x 0.4 mm thickness with a resonance frequency of 450 kHz. These PZTs are a material called SM111, which is a modified form of PZT-4. Comparisons of material properties provided by the company are shown in Table 1. To avoid damaging the PZTs with heat, wires were attached to the positive and negative electrode of the PZTs by the company. I used a free cross-platform ultrasound simulation toolbox to write a code that calculated the radius of curvature and number of PZT elements to incorporate in my phased array based on the desired focal point (FOCUS). The results are displayed in Figure 3.

Table 1: PZT Material Properties Comparison

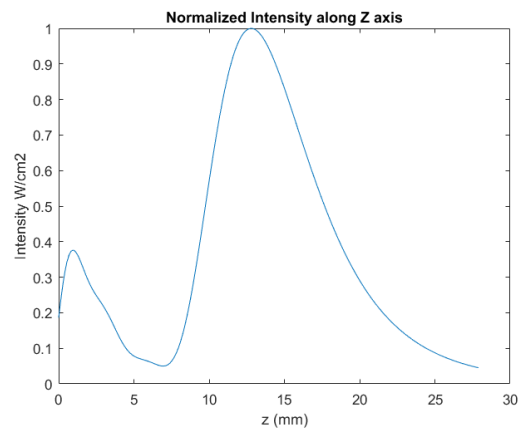
Property	Unit	Symbol	PZT-4	Modified PZT-4
Electromechanical Coupling Coefficient		K_p	0.54	0.58
		K_t	0.43	0.45
		K_{31}	0.32	0.34
Piezoelectric Constant	$\times 10^{-12} \text{ m/V}$	d_{33}	300	320
		d_{31}	-130	-140
	$\times 10^{-3} \text{ Vm/N}$	g_{33}	26.4	25
		g_{31}	-12.9	-11
Dielectric Constant	@1kHz	$\epsilon \text{ (F/m)}$	1300	1400



(a)



(b)



(c)

Figure 3: FOCUS generated simulations. (a) Geometry for phased array. (b) Normalized intensity field based on phased array geometry. (c) Normalized intensity along the z axis to simulate the location of the focal region from the center of the transducer. The depth of the transducer was modeled to be 4 mm.

2.1.3. Transducer Geometry

Based on the location of the vagus nerve from the surface of the skin in rats, the focal point was selected to be approximately 10 mm. This value was collected during Wasileczuk's animal studies from her surgical assistants. I ran simulations and recorded measurements with 0 mm representing the center of the transducer. The final distance from the center of the transducer to the end of the transducer was 4 mm, so the focal region was represented in simulations as 14 mm. With help from Kevin Buno, a graduate student in the biomedical engineering department, I designed the shape of the transducer in SolidWorks and 3D printed the component on campus using an Ember 3D Printer (AutoDesk). All prints were done with 1x1L standard clear prototyping resin, XY resolution of 50 microns, and Z resolution of 10 microns. To account for the porous qualities of the 3D printed concave disc I treated the component with acetone. Figure 4 shows the design of the concave disc with nine inserts for the PZTs to be secured into with epoxy and silicone. Table 2 is a list of the final transducer design decisions.

Table 2: LIFU Transducer Dimensions

PZT Material	Modified PZT-4
PZT Diameter x Thickness	0.5 mm x 0.4 mm
Resonance Frequency	450 kHz
Number of PZTs	9
Focal point from end of transducer	10 - 12 mm
Outer Diameter	22 mm
Inner Diameter	20 mm
Radius of Curvature	14.5 mm

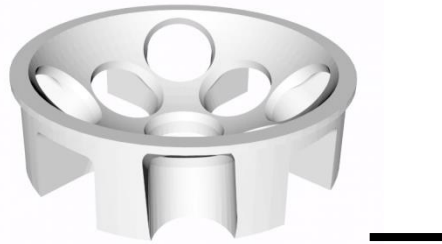


Figure 4: SolidWorks design of transducer geometry. Scale bar = 5 mm.

2.1.4. Backing and Matching Layer

For the backing and matching layers, I chose medical grade silicone (NuSil MED2-4420) and medical grade epoxy (Loctite® M-31CL™ Hysol®), respectively, based on literature and availability. Wearing nitrile gloves, I carefully placed three PZTs at a time into their slots and applied the silicone backing to hold them in place. The silicone cure time was three minutes and did not require any heat that would compromise the PZT characteristics. Identified by literature,

the optimal matching layer of $\lambda/4$ meant that I needed to apply an even layer of 0.88 mm onto the concave disc. I rounded down to 0.8 mm to allow for 0.08 mm of tolerance. To achieve this even layer, I first modified my SolidWorks design of the concave disc by removing all of the PZT slots. I then added a 0.8 mm thickness to the design and 3D printed it. Using this component, I next used mold putty, which epoxy would not adhere to, to create the negative mold to form an even layer of epoxy onto the face of my transducer. A schematic of the matching layer procedure is represented in Figure 5. The “Amazing Mold Putty” is FDA-compliant 1:1 ratio silicone mold putty that was hand mixed and cured in 20 seconds (Alumilite). I put epoxy into the concave disc with the exposed PZT elements and then pressed the negative mold on top. This fixture of the concave disc and positioned negative mold was left overnight because the epoxy has an 18-hour cure time at room temperature. When the mold was removed, a 0.8 mm cured layer of epoxy was present. This was verified by grinding down the 3D printed test concave shape as seen in Figure 6.

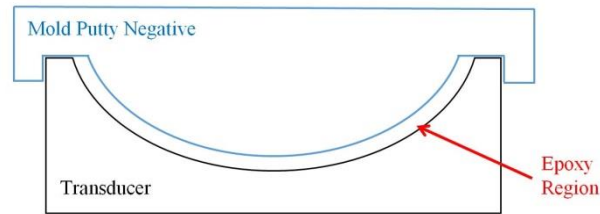


Figure 5: Setup for applying a specific matching layer thickness to transducer

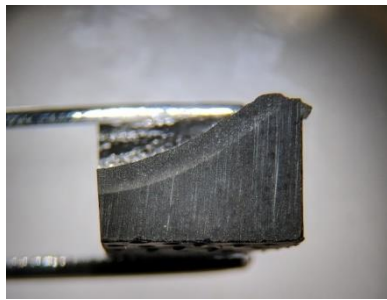


Figure 6: Cross-sectional view demonstrating even application of matching layer

2.1.5. Matching Network

The driving force behind the development of the matching network calculations and associated MATLAB code was Christian J Colon Ortiz from Dr. Juan García’s lab. We selected a matching L network to deliver maximum power to the load from the source with an impedance of 50 ohms (Z_0). Referencing Figure 7, there are two different circuit layouts based on how the load impedance compares to the source impedance. There are eight potential combinations of capacitors and inductors for this type of matching network. To narrow down the selection, I measured the Z (Z_{PZT}) and theta (θ_{PZT}) values of each PZT with an E4980A Precision LCR Meter (Agilent) at 450 kHz. Specifically, the impedance of the PZTs set in the concave disc with

the backing and matching layer applied were used in the calculations. I assigned each PZT an ID to keep track of the impedance and matching network values associated with it. Based on a simplified Van Dyke's Model and recorded measurements, we modeled the PZTs as a resistor and capacitor in series.

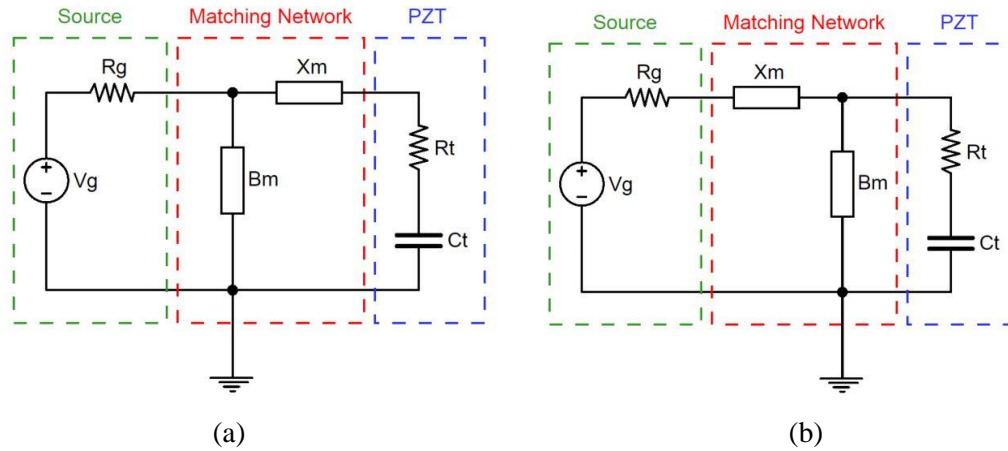


Figure 7: Matching L Networks for eight potential combinations of inductors and capacitors. (a) Network used when impedance of transducer is less than impedance of source. (b) Network used when impedance of transducer is greater than impedance of source.

The calculated PZT impedances were greater than the 50 ohm source impedance. As such, this narrowed the potential matching network layouts to those having the transducer in series with the first reactive component then in parallel with the next reactive component. The remaining four combinations were made up of inductors and capacitors (Table 3). Case 1 and Case 2 were the chosen layouts.

Table 3: Potential combinations of inductors and capacitors for matching L network

Combinations	Series X_m Component	Shunt B_m Component
Case 1	X_L	B_C
Case 2	X_C	B_L
Case 3	X_C	B_C
Case 4	X_L	B_L

Between the last two combinations of capacitor or inductor for the shunt (B_m) or series (X_m) value, the network was chosen based on availability of reactive components' values on Digi-Key. Equations 14 – 17 show how the series and shunt components were calculated for. A more in-depth break down of the matching network calculations has been covered by other researchers [39],[57],[96].

$$R_t = Z_{PZT} * \cos(\theta_{PZT}) \quad (14)$$

$$X_t = Z_{PZT} * \sin(\theta_{PZT}) \quad (15)$$

$$B_m = X_t \pm \frac{\sqrt{\frac{R_t}{Z_0}} * \sqrt{R_t^2 + X_t^2 - Z_0 * R_t}}{R_t^2 + X_t^2} \quad (16)$$

$$X_m = \frac{1}{B_m} + \frac{X_t * Z_0}{R_t} - \frac{Z_0}{B_m * R_t} \quad (17)$$

Colon Ortiz wrote a MATLAB code to calculate the impedance and graphical representation of the resonance frequency that each of the two combinations would give based on readily available values. The overall efficiency of each matching network was calculated for using Equations 3 – 8.

2.1.6. Power Amplifier

The radio frequency (RF) power amplifier I chose was based on size, price, and availability. I ordered this 4.5 mm x 4.15 mm x 1.50 mm amplifier off of Digi-Key for \$1.88. The frequency range and number of components needed for the external network narrowed the search down. The MMG3H21NT1 from NXP is internally matched at 50 ohms, can be used at 450 kHz, needs a single 5 volt supply, and has a small signal gain of 19.3 dB. The application circuit values were provided by the company, listed in Table 4, after I contacted them and told them what frequency range (450 kHz) I was operating in (Figure 8).

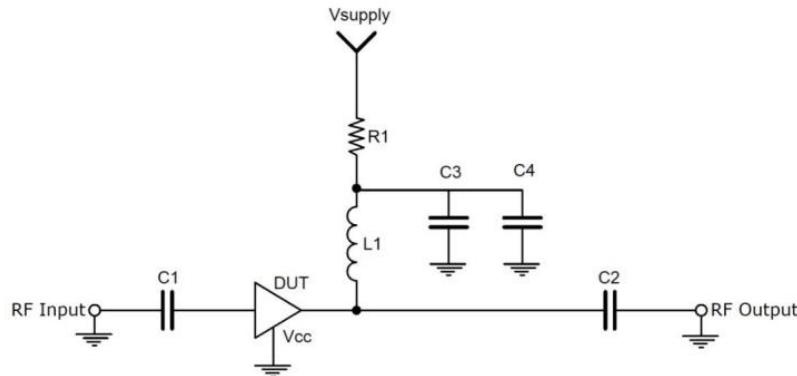


Figure 8: 50 Ohm Application Circuit Schematic for 450 kHz

Table 4: 50 Ohm Application Circuit Values for 450 kHz

Part	Description
C1, C2, C4	1 μ F
C3	0.1 μ F
L1	33 μ H
R1	0 Ω

2.1.7. PCB Design

I used an open source EDA software to create my PCB circuit schematics and layouts (KiCad EDA). CID has a LPKF ProtoMat@S100 circuit board plotter for in-house rapid PCB prototyping that I used (LPKF). I fabricated PCB boards containing matching networks for each PZT on one side and the amplifiers with their external networks on the other side. To help with heat dissipation, I designed and implemented a large, shared ground plane between the amplifiers and placed a heat sink over the amplifiers with adhesive tape. I soldered on the surface-mount device (SMD) components and pin outs under a microscope with Chip Quik® lead free low temperature solder paste (SMDLTLFP10T5) and a hot-air rework station 303D (Sparkfun) set at 220°C. The pin outs were for power, input signal, and ground. The positive and negative wires of each PZT were soldered to their specific matching network and amplification channel.

2.2. Bench Top Characterization

A E3630A triple output DC power supply (Agilent) was set at 5 volts and 12 volts to respectively power the device and the TC4038 hydrophone (Teledyne Reson) VP1000 voltage preamplifier (Reson). The voltage preamplifier was set to a 50 kHz high pass filter with a 32 dB gain. The 33522A function waveform generator (Agilent) supplies a 450 kHz sine wave with varying amplitudes. The transducer was submerged in deionized water in a rubber lined container (Figure 9). When the input signal and power source were turned on, the amplitude recorded from the hydrophone was displayed on the MS0734B mixed signal oscilloscope (Agilent). I measured pressure at various locations and amplitudes. I created a 8 mm x 20 mm 2D intensity map of the FUS beam starting from the edge of the transducer and evaluating the x and z axis. I measured in 2 mm increments to 20 mm in the z direction. I measured in 2 mm increments from -4 mm to 4 mm in the x direction. The 0 mm point represents the middle of the transducer.

When the intensity map was created the focal region was further characterized. The focal region evaluated was a 2 mm x 4 mm region at 10 mm to 12 mm from the center of the transducer. I created intensity maps of the focal region and varied the amplitude from -6 dBm to 9 dBm. I selected the amplitude parameter of -3 dBm based on the shape and location of the focal region. The type of intensity reported was instantaneous intensity. To evaluate the potential of beam steering for future iterations, I disconnected three of the PZTs and created a 10 mm x 20 mm intensity map of the shifted FUS beam.

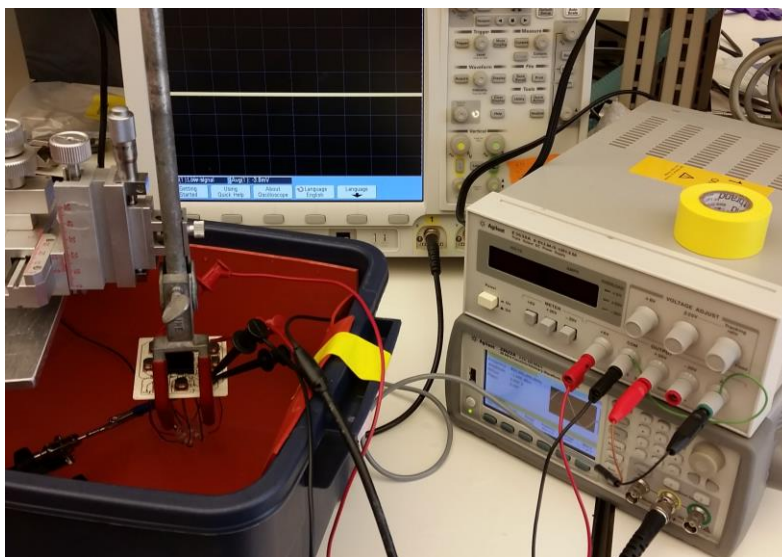


Figure 9: Bench top test setup for measuring the amplitude of the soundwaves with a hydrophone. The hydrophone was secured in place and the LIFU device was moved in the x and z axis using a stereotactic frame.

2.3. Surgical Overview

2.3.1. Surgical Setup

To measure the effect of the LIFU therapy on the modulation of cytokines, *in vivo* rat experiments were performed with the assistance of Wasilczuk and Albors as the surgeons. We used 12 male 200 - 300 gram Sprague-Dawley rats. All surgical procedures were approved by the Purdue Animal Care and Use Committee (PACUC). The rats were first anesthetized with 4 – 5% isoflurane so that we can weigh and shave the rats in the regions of surgical interest. At the beginning of each surgery, we gave the rats an intraperitoneal (IP) injection of 0.04 mL butorphanol. I immediately administered an induction IP injection of ketamine-xylazine (ket/xyl), a mixture of 75 mg/kg ketamine and 5 mg/kg xylazine. Throughout the experiment, the rats were placed on a heated surgical mat and supplied with oxygen at 2 L/min. Every 20 minutes, we gave a maintenance IP injection of ket/xyl.

2.3.2. Pre-Made LPS Procedure

To induce endotoxemia, we IP injected an LPS-saline mixture (5 mg/kg). LPS arrived in a 100 mg glass bottle from Sigma Aldrich. Jennifer Sturgis from Robinson's lab helped us prepare pre-made LPS for the animal study. We first mixed 15 mL of saline into the glass bottle containing the 100 mg of LPS. We transferred this amount to a polypropylene tube. We injected another 5 mL of saline into the glass bottle. The glass bottle and polypropylene tube were sonicated for 30 minutes. We transferred the remaining 5 mL of saline to the polypropylene tube to be sonicated for another 15 minutes. We aliquoted 0.4 mL of the LPS saline solution into Eppendorf tubes that were then placed in a frost free freezer. Before each surgery we weighed

each rat and calculated the amount of LPS needed. Based on the result we pulled out the number of prepared tubes before the experiment. We sonicated the tube for 30 minutes and then pulled the specific amount needed for injection. This process ensures that the dosage was consistent for each surgery.

2.3.3. Surgical Timeline

To ensure that the left cervical vagus was receiving the full stimulation, the surgeons exposed it with a 20 mm incision on the neck of the rats. They also exposed and inserted a catheter into the left leg of the rat for blood collections, which occurred in 30 minute intervals. To avoid the formation of blood clots in the line, we flushed the catheter with heparinized saline every 15 minutes. We took the first blood collection following the exposure of the vagus and catheter insertion. This collection represented the baseline sample and is denoted as time point “-30 minutes”. Thirty minutes later represents time point “0 minutes” and was when I injected the LPS. No blood was taken at this time point. To minimize experimental variability, I performed all of the LPS injections throughout the animal studies.

After the LPS injection, I setup the LIFU device for VNS. I applied ultrasound gel (Aquasoinc 100) to the incision site, which provided a medium for the ultrasound waves to travel through from the transducer to the vagus nerve (Figure 11). I carefully situated the transducer head above the target and then pressed it up against the rat’s neck. The device was held in place with alligator clips attached to a base by flexible arms. The power supply and function generator were connected to the PCB board. I took the second blood collection at time point “30 minutes” and then immediately turned the LIFU device on for a total of 5 minutes. In thirty minute increments four more blood samples were taken to show the effect of stimulation on the cytokine levels. A total of six blood samples were collected. A detailed timeline of the surgery can be found in Figure 10. Immediately after collection, each sample was placed on a rocker until they were picked up for flow cytometry analysis done on campus by Paul Robinson’s Flow Cytometry Lab. At the end of the experiment, we euthanized the rat with 0.9 mL of beuthanasia.

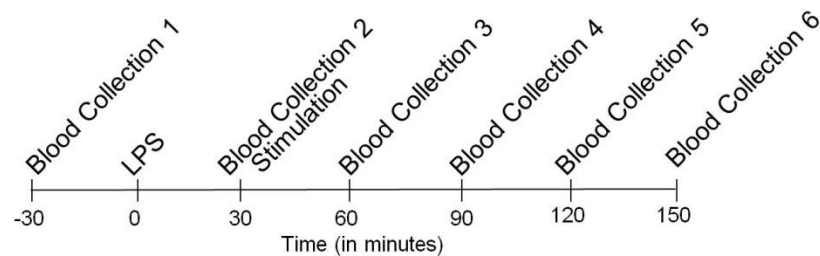


Figure 10: Surgical Timeline

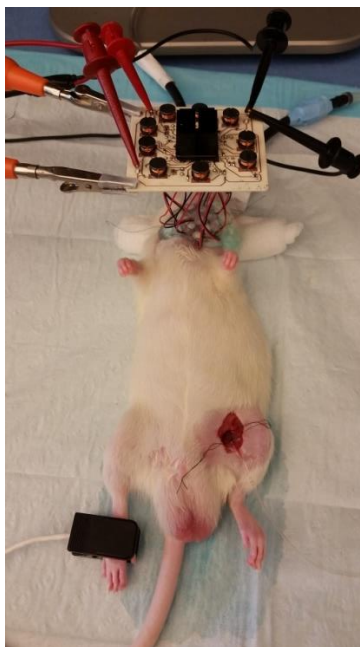


Figure 11: Surgical setup of rat with LIFU device positioned over the vagus nerve and a left leg catheter for blood collection.

2.3.4. Flow Cytometry

We collected the blood in 300 μ L K2 EDTA coated vials. After Robinson's lab received the vials, they centrifuged the samples and removed the plasma. They performed a LEGENDplexTM Rat Inflammation Panel assay using fluorescent beads coated with antibodies for specific analytes. The cytokines of interest are IL-6, IL-10, and TNF- α . The concentration of each specific cytokine was found through measuring the analytes present with flow cytometry. Two replicates and an average of the concentration are reported for each time point.

2.3.5. Surgical Considerations

The control rats used for this study received LPS, but no therapy. I used control data from Wasilczuk's animal studies because our experimental procedures only differ in the type of therapy applied. I compared the effect of my LIFU device therapy against the control data.

I filled out surgical logs detailing the events of each animal surgery. Based on issues that involved LPS injections or breathing the data was removed from the study. Breathing issues included rats that did not handle the ket/xyl well and as a result, had elevated heart rates throughout the experiment or stopped breathing and had to be revived.

2.4. Statistical Analysis

I consulted with Wasilczuk and Ahmad Hakeem Abdul Wahab, from the Purdue University Statistical Department, on the statistical analysis of my results. Rats that received

therapy from the LIFU device are designated with the FUS label. We plotted the average TNF- α concentration of the controls against the average of the FUS rats for each time point. We next conducted a Cohen's h analysis to determine the peak concentration of TNF- α . We observed a peak concentration at time point "90 minutes" and identified this as the point of analysis. At that time point the TNF- α concentration of each FUS rat was plotted alongside the average control TNF- α concentration data. To identify which rats did not respond to the therapy we used the statistical package SAS 94 to calculate the studentized residuals. Finally, we performed a two-sample t -test, with an $\alpha = 0.05$, between the controls and the rats that responded to the therapy. If the P value was less than 0.05, the results were considered statistically significant.

3. RESULTS

3.1. Geometric Comparison

The images and dimensions of the final LIFU device design are presented in Figure 12. The final design consisted of a transducer, matching network, and amplification network. With the heat sink and transducer the device is 50 mm x 57 x 76 mm.

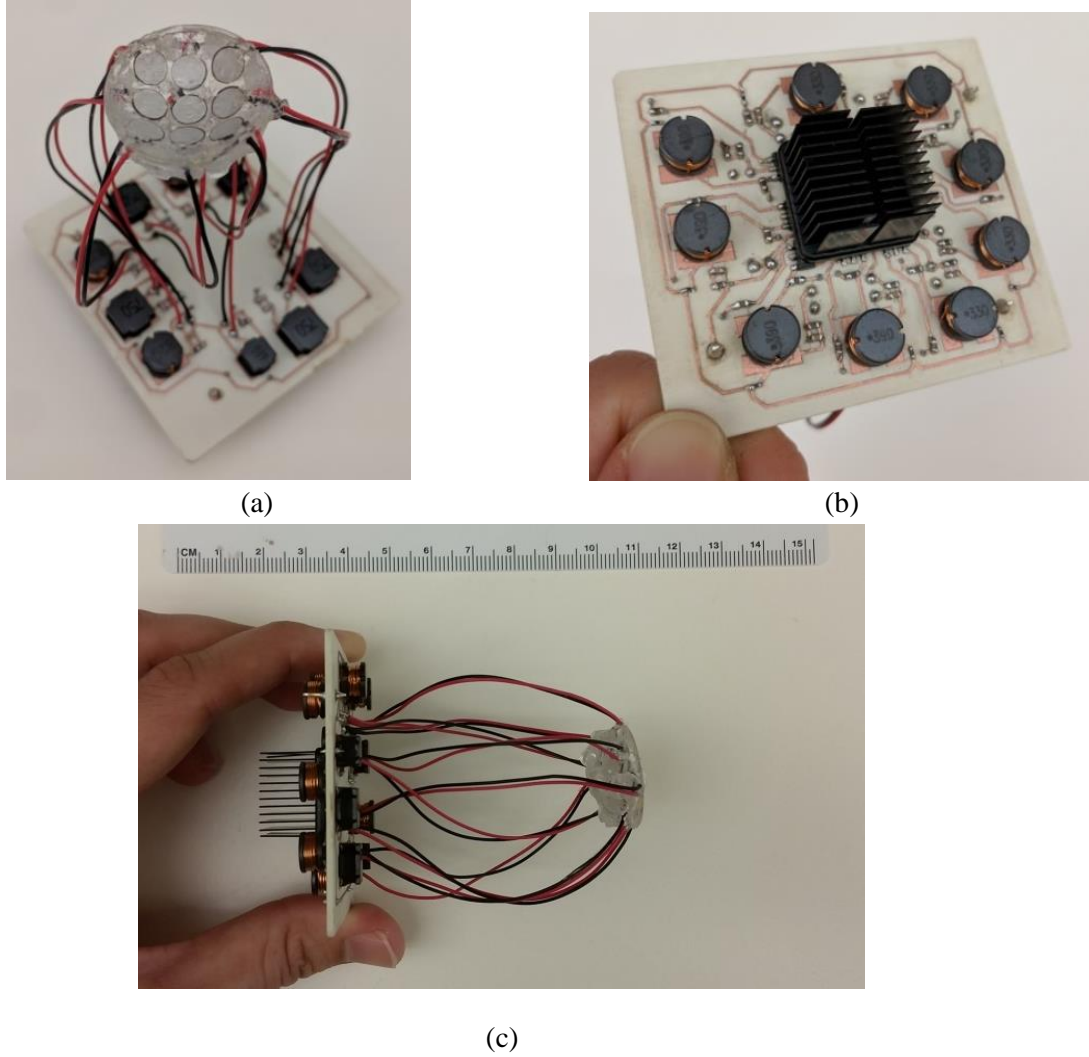


Figure 12: (a) Final LIFU Device Design. (b) Amplification network with heatsink over nine amplifiers. (c) Final dimensions of 50 mm x 57 mm x 76 mm.

A comparison between the H-115 system and the LIFU device is presented in Figure 13. This image shows the transducer, coupling cone, matching network, and amplifier that make up the H-115 system.



Figure 13: System comparison of H-115 and LIFU device: transducer, matching network, and amplification network. The six inch ruler was included for reference.

3.2. Price Comparison

A price comparison between the H-115 system and the LIFU device are presented in Table 5 and Table 6. The price breakdowns pertain to the transducers, matching networks, and amplification networks. A further break down of the LIFU components is located in Table S4 and Table S5. The total cost of the H-115 system is \$9,835 and the total cost of the LIFU device ranges from \$80 to \$232.84. A range is provided for the LIFU device because the price is dependent on material choice and availability.

Table 5: Bill of Materials for H-115 System

H-115 System	Price (\$)
PZT Element	\$4,250.00
Matching Network	
Coupling Cone	\$685.00
AE 7224 Amplifier	\$4,900.00
Grand Total (\$)	\$9,835

Table 6: Bill of Materials for LIFU Device

LIFU Device	Component	Vendor	Price (\$)
Transducer	PZT Elements	STEMiNC	29.00
	*Silicone	Nusil	100.50
	*Epoxy	Henkel	20.00
	*Mixing Tips	McMaster-Carr	11.40
	*Mold Putty	Alumilite	20.00
Matching Network	Inductors	Digi-Key	6.79
	Capacitors	Digi-Key	10.00
Amplification Network	Amplifiers	Digi-Key	18.76
	Heatsink	Digi-Key	5.66
	Inductors	Digi-Key	5.47
	Capacitors	Digi-Key	5.26

*CID Resources

**Full price break down in Table S4 and Table S5.

Grand Total (\$)	232.84
In-House Total (\$)	80.94

3.3. Matching Network Development

The measured and calculated values for the nine PZTs are presented in Table 7. The impedance values I recorded represent the values of the PZTs after they had been incorporated into the transducer. I used the impedance values to calculate the potential values for the series and shunt components (Table 8). The potential combinations of the values are presented in Table 3. The final values I selected and their calculated power transfer efficiency are presented in Table 9. A graphical representation of the power transfer efficiency and resonance frequency for one of the PZTs is presented in Figure 14.

Table 7: PZT Impedance Characterization

PZT ID	Z (ohms)	Theta (degrees)	R _t (ohms)	C _t (nF)
A1	910.40	-51.70	564.25	0.50
A2	887.70	-50.09	569.53	0.52
A3	863.70	-45.08	609.87	0.58
B1	890.40	-52.20	545.73	0.50
B2	775.70	-47.76	521.45	0.62
B3	713.70	-45.60	499.35	0.70
C1	967.20	-52.90	583.42	0.46
C2	842.40	-46.80	576.66	0.58
C3	911.50	-48.04	609.44	0.52

Table 8: All potential inductor and capacitor values for series X_m component and shunt B_m component

PZT ID	Series X_m Component		Shunt B_m Component	
	X_L (μH)	X_C (nF)	B_L (μH)	B_C (nF)
A1	94.2	1.33	78.8	0.98
A2	91.3	1.37	76.9	1.01
A3	85.7	1.46	74.0	1.11
B1	93.7	1.34	78.0	0.98
B2	83.1	1.51	70.4	1.10
B3	77.9	1.61	66.5	1.17
C1	98.6	1.27	82.2	0.94
C2	85.9	1.46	73.5	1.09
C3	90.6	1.38	77.3	1.04

Table 9: Final shunt inductor and series capacitor values for case 2 combination of series X_c and shunt B_m components and the calculated power delivered.

PZT ID	X_C (nF)	B_L (μH)	Power Delivered (%)
A1	1.3	82	99.734
A2	1.4	75	99.908
A3	1.4	75	99.961
B1	1.4	75	99.781
B2	1.5	68	99.914
B3	1.6	68	99.918
C1	1.3	82	100.000
C2	1.4	75	99.934
C3	1.4	75	99.895

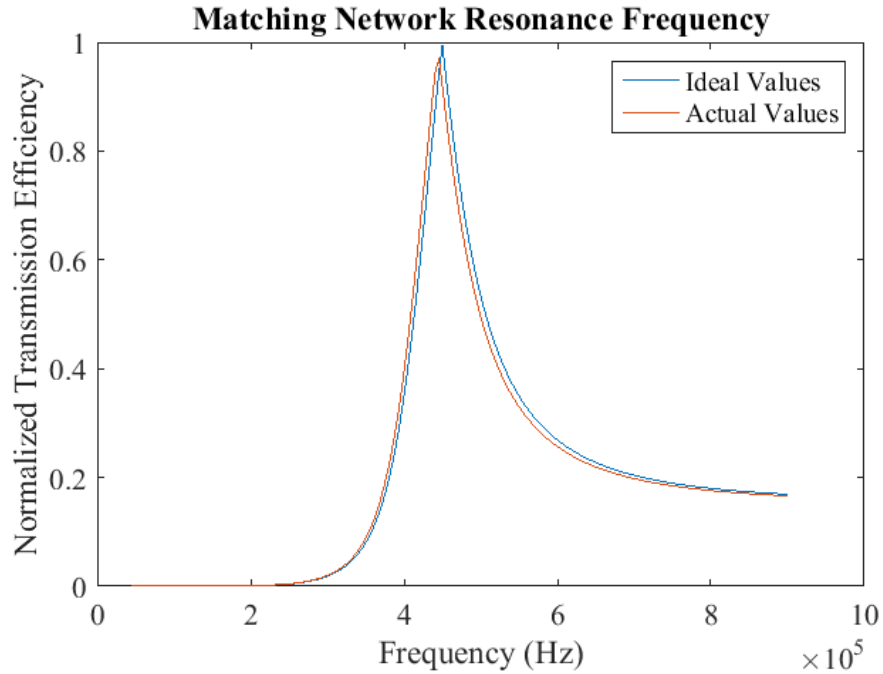


Figure 14: Graphical representation of ideal vs actual components selected for matching network

3.4. LIFU Device Characterization

I created a 2D plot of the intensity for the characterization of the LIFU device (Figure 15). The shape of the focal region was 1 mm x 4 mm and occurred between 10 mm and 12 mm from the transducer. I disconnected three of the PZT channels and demonstrated a shift in the focal region (Figure 16). The shape of the focal region was 1 mm x 1 mm and occurred between 10 mm and 14 mm from the transducer. The general focal region identified, when all of the PZT channels were operating, was 4 mm x 2 mm at 10 mm to 12 mm from the transducer. I evaluated the focal region further by varying the amplitude from -6 dBm to 9 dBm. Figure 17 shows the progression of the focal region shape and location based on the amplitude variations.

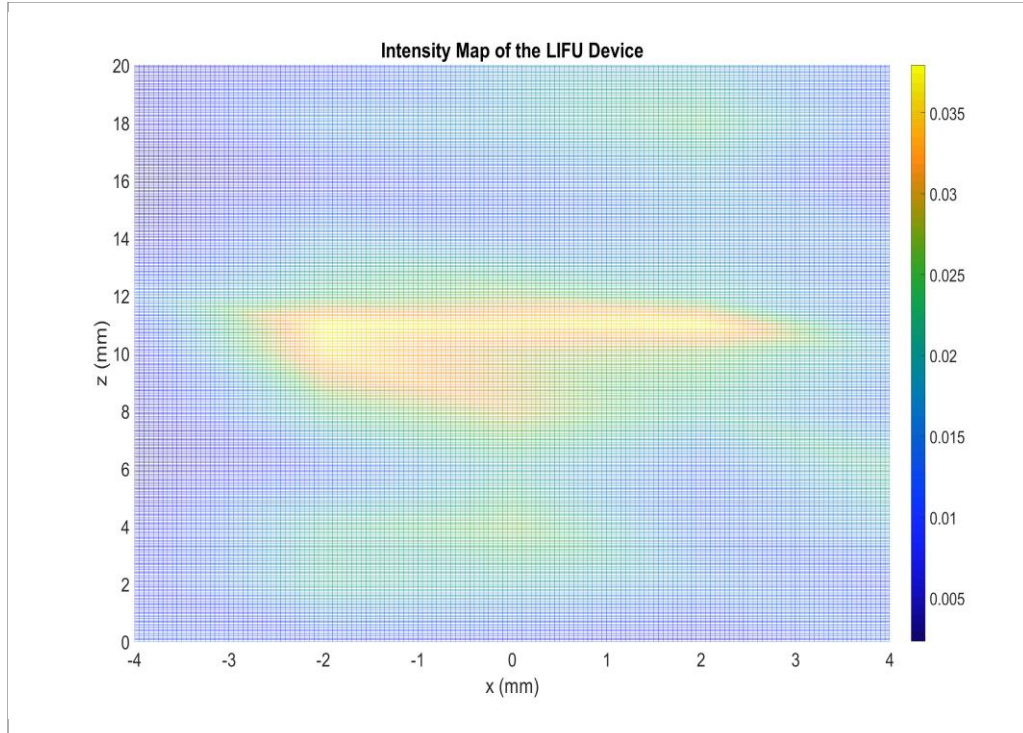


Figure 15: 2D intensity map of the LIFU device at -3 dBm. The focal region was 1 mm x 4 mm and occurred between 10 mm and 12 mm from the center of the transducer. The color bar represents the intensity in W/cm^2 .

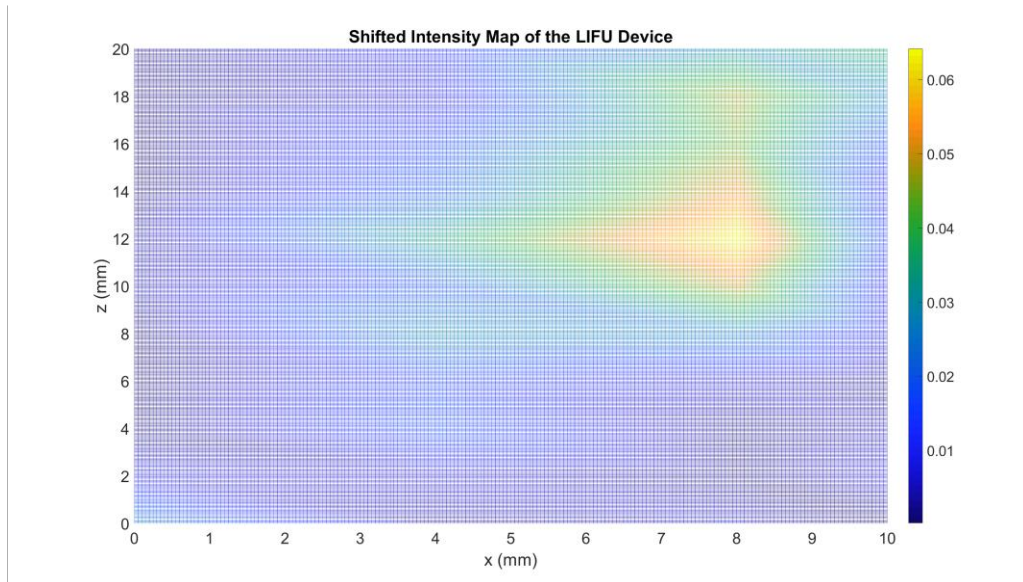


Figure 16: 2D intensity map of the LIFU device at -3 dBm. The focal region was shifted 8 mm from the center of the transducer. The focal region was 1 mm x 1 mm and occurred between 10 mm and 14 mm from the center of the transducer. The color bar represents the intensity in W/cm^2 .

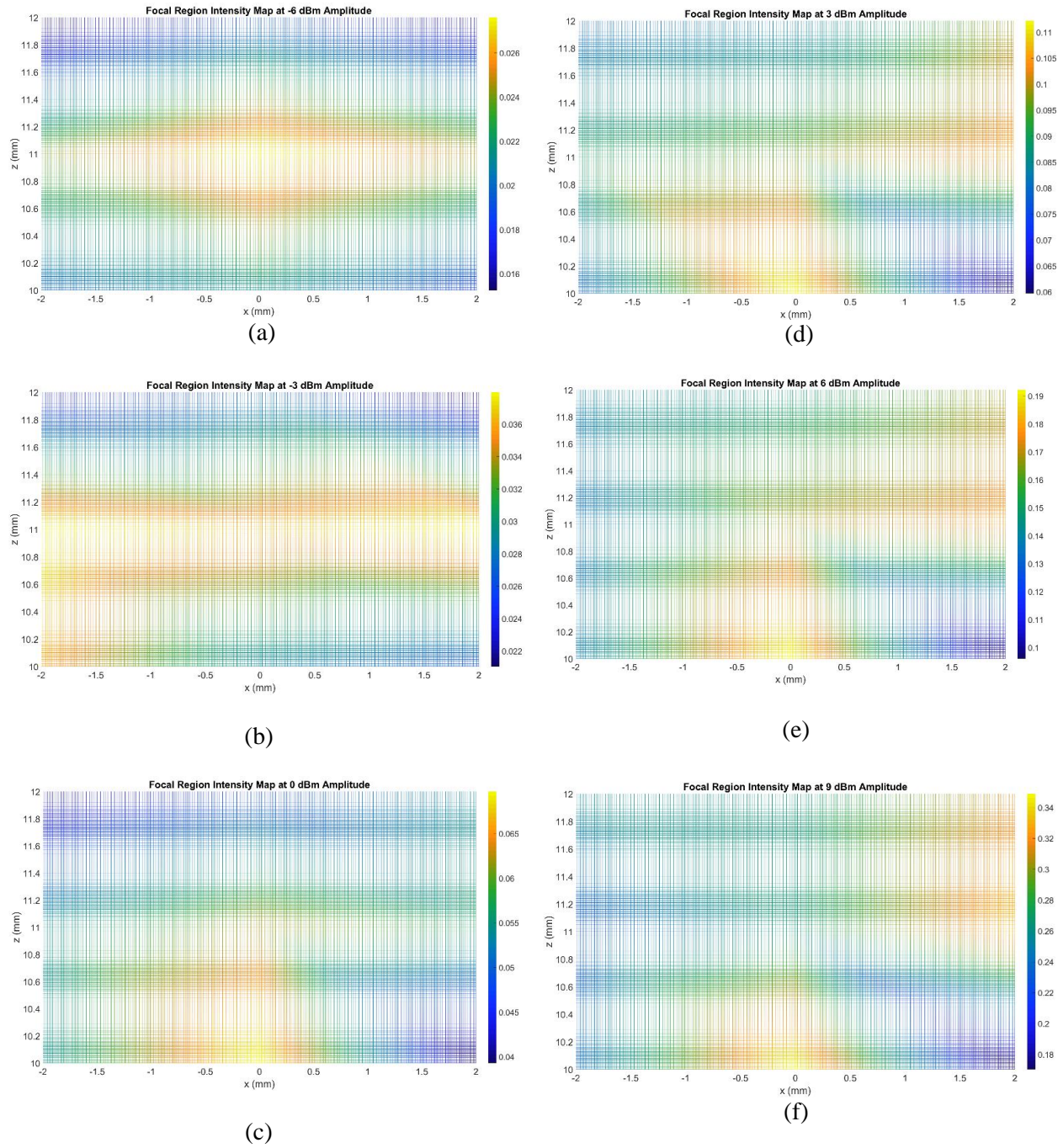


Figure 17: A focal region of 4 mm x 2 mm was evaluated 10 mm to 12 mm from the center of the transducer. At this position the amplitude was varied from -6 dBm to 9 dBm. The focal region shape and location varied based on the amplitude. The color bar represents the intensity in W/cm^2 .

3.5. Animal Study

The animal study we conducted evaluated the concentration of TNF- α . We identified time point “90 minutes” as the peak concentration of TNF- α in Figure 18 and this was further confirmed with the Cohen’s h analysis (Figure 19 and Table 10). Cohen’s h proportional analysis was used to identify where meaningful differences were between the controls and the FUS data. Figure 20 represents the data recorded at time point “90 minutes.” The average for the controls and the average for each FUS rat are presented in Figure 20. Each FUS data bar was the average of two replicates received from the flow cytometry process.

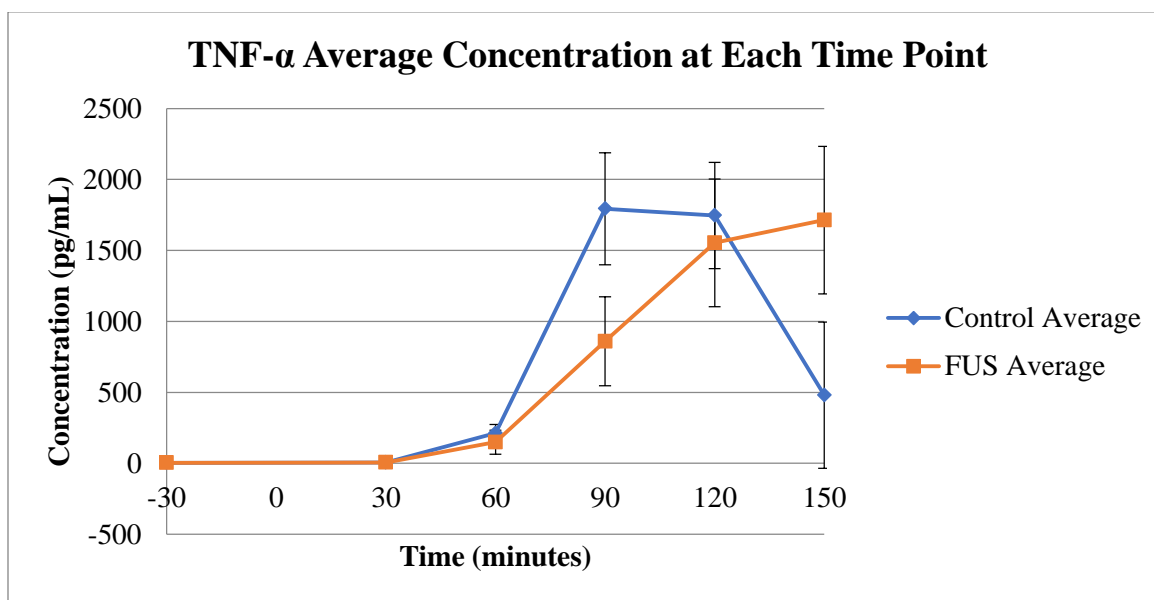


Figure 18: TNF- α average concentration data for 8 rats that received therapy from the LIFU device and 5 rats that did not receive therapy. Based on events recorded in the surgical logs, 4 of the FUS rats were removed from the study.

Table 10: A meaningful difference between the Cohen’s h proportions can be deemed small (greater than 0.2), medium (greater than 0.5) or large (greater than 0.8).

Time	Difference
-30	0.07
30	0.20
60	0.63
90	0.47
120	0.03
150	0.35

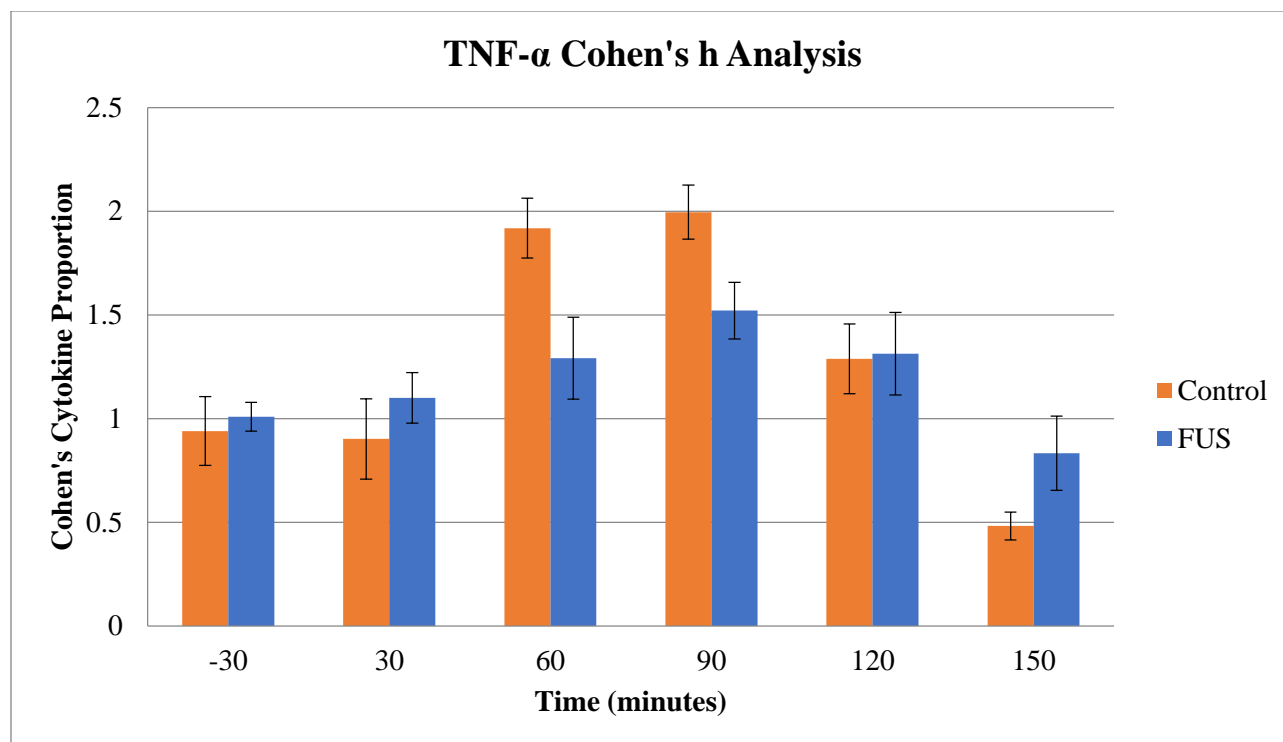


Figure 19: Cohen's h proportional analysis of the three cytokines TNF- α , IL-6, and IL-10.

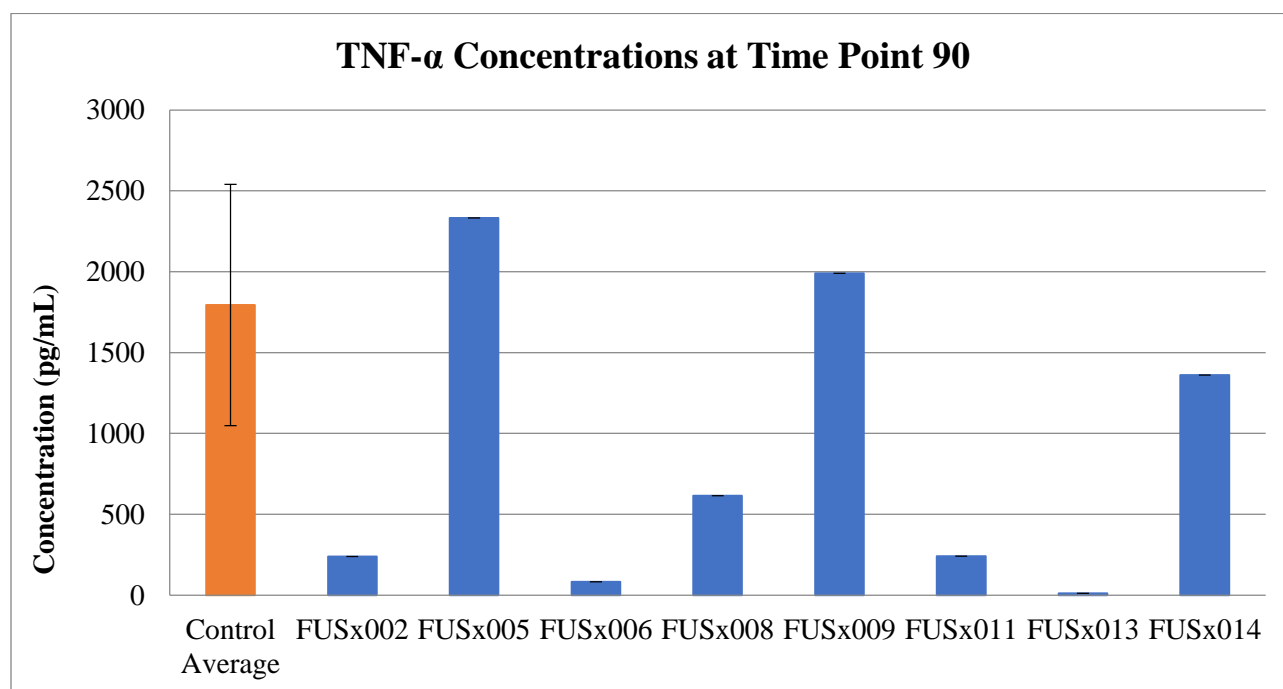


Figure 20: Evaluation of therapies at time point “90 minutes” for controls and the LIFU device. There was an $n = 5$ for control data. Error bar for the control represents standard deviation. Each FUS label represents one rat. There are no error bars for the FUS data because the data is represented as the average of two replicates.

4. DISCUSSION

4.1. LIFU Design Goal Overview

The goal was to design and fabricate a LIFU device based on the parameters of cost, size, and consolidation of accessory electronics. A price range of a few hundred dollars was set. I wanted to eliminate the need for expensive equipment, such as an amplifier. The goal was to design a PCB circuit board that would contain a matching and amplification network for the transducer. It was important to consider power consumption, but it was difficult to set a specific parameter when LIFU device studies do not report it and HIFU device studies do not prioritize it. LIFU device studies are more focused on the biological response of the therapy and will use established FUS systems. HIFU studies that focus on the fabrication of the device will report power consumption, but they are operating at such extreme intensities an industrialized amplifier is typically chosen over building their own amplification network. However, I did reference many HIFU studies for the fabrication of my device because they were highly detailed on their design processes for the transducer and matching network.

Design considerations were based on issues that arose when Wasilczuk and I used the H-115 system in animal studies. The experiments were performed on 200 – 300 gram Sprague-Dawley rats. The transducer diameter needed to be less than the size of the rat's neck. When pressed up against the neck of a rat the focal region of the beam needed to occur at approximately a 10 mm depth, where the vagus nerve is located. This design specification arose from issues with maneuverability of the H-115 transducer. The diameter of the PZT element is 64 mm with a focal length of 40 mm. The focal length is where the focal region occurs with respect to the face of the PZT element. With such a large device it is difficult to aim for a rat's nerve, but with the coupling cone the user only needs to measure a distance of 10 mm from the end of the cone to the target. The coupling cone is attached to the PZT element, filled with water, and has an opening where a cover, secured with an O-ring, is placed over. Ultrasound gel is then placed between the end of the cone and the target. The water and gel provide a bridge for the ultrasound to travel through. Due to the extreme focal length, the H-115 system needs to be mounted and precisely placed, using a stereotactic frame, before stimulation (Figure 21). It was important to build a device with a transducer head that that would press directly against the skin without the use of a coupling cone. In Wasilczuk's animal studies the H-115 system operates at 250 kHz and targets the vagus nerve with an I_{SPTA} of 2.3 W/cm^2 . My device needed to produce a FUS shaped beam with an intensity that could induce a therapeutic effect in the animal study.

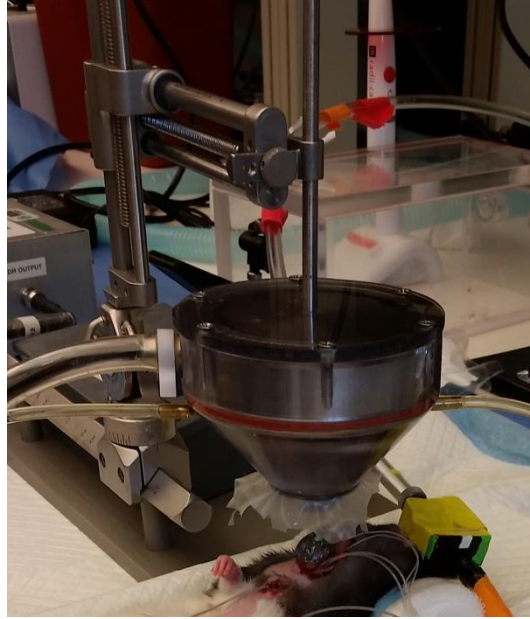


Figure 21: H-115 Transducer with coupling cone mounted and positioned over the vagus.

4.2. PZT Shape Considerations

Many LIFU studies focus on the biological response of their therapy as well as how the device affects tissues surrounding the focal region [89], [97]–[99]. These studies often employ the use of a single-element PZT, a function generator, and an amplifier. The single-element is typically curved and purchased from a manufacturer. I first reached out to Sonic Concepts, the manufacturer of the LIFU device we had on loan. They had many therapeutic transducers available in a variety of sizes and frequencies. However, the price quotes were for thousands of dollars and the accessories, such as the coupling cone, were well above my target budget (Figure 22).



Figure 22: H-115 Transducer, Coupling Cone, and Matching Network

Since these transducer systems came with the matching network, I decided to contact multiple PZT manufacturers about purchasing just a curved PZT element that was capable of operating at a low frequency, had a small diameter, and had a focal point of about 10 mm. After consulting with the sellers, I learned that my design requirements (specifically a small diameter, curved PZT element) would require a customized PZT element, which was quoted at \$300 to \$500 for each element with a minimum purchase order of ten. My next attempt was to purchase a pre-made curved PZT element or get a free sample of a curved PZT element from a vendor, but I did not receive a response or was unable to find a reasonably priced element. Souris *et al* used a CNC machine with a grinding spindle, equipped with diamond tools, to shape a piece of bulk PZT element into their desired curved shape. However, the inner and outer surfaces needed to be silvered to create electrodes for polarizing the element. During this silvering process, a high voltage is applied between the electrodes above the Curie temperature [48]. Due to the difficulty of that process, this portion of the work was finished off by a manufacturer. I did not consider this option because I did not want to use a PZT manufacturer for customization of any portion of my project based on the correspondences I had with them in terms of pricing and minimum quantity requirements. An alternate approach was to purchase pre-made, ready to use PZTs elements, which are available in discs, rods, and cylinders at set frequencies. My solution was to use premade PZT discs to build a curved phased array. This gave me the flexibility of determining my transducer dimensions and the curved shape I needed to geometrically achieve the desired focal region, without going over budget.

4.3. PZT Material Considerations

I used the company STEMiNC because of their wide selection of PZT disc frequencies and sizes. I purchased ten PZT discs for \$29.00 with the desired specifications of low frequency (kHz range) and small diameter (5.0 mm x 0.4 mm). A common PZT material type is called PZT-4, which is a type of Navy I PZT and is considered to be a material with “hard” characteristics. When operating at resonance, most PZT elements will generate heat, however this class of PZT elements has a very low loss factor, making it a good candidate for low power consumption [48],[55],[75]. Other parameters to consider for PZTs are their d -coefficients, g -coefficients, piezoelectric coupling factor k , and the dielectric constant ϵ (F/m). Materials used for vibrational applications, such as actuators, have higher d -coefficient values. Materials that produce voltage in response to mechanical stress, such as sensors, have higher g -coefficient values. The electromechanical effect is characterized by the piezoelectric coupling factor k . The charge from the voltage is stored on the electrode material and is measured by dielectric constant ϵ (F/m). The PZT element I purchased is a modified version of PZT-4. It has higher d -coefficients, higher k value, higher ϵ , and lower g -coefficients, as seen in Table 1. These properties are ideal because my LIFU device is not a sensor and I want to maximize the vibrational effects for ultrasound intensity.

4.4. Matching Network Considerations

It was specified by the manufacturer that the PZT elements would be within ± 10 kHz of 450 kHz. It would be unrealistic to expect nine PZT elements, for the price of \$29.00, to have the exact same piezoelectric qualities or for those impedance values to not change after being incorporated into the transducer. Even though the PZTs were not exactly at the target resonance frequency, I still took impedance measurements at 450 kHz because that was the frequency I ran all of my experiments at.

From the impedance values, Christian and I were able to calculate the ideal capacitor and inductor values from a code he wrote in MATLAB. Table 8 shows all of the potential capacitor and inductor values that could be used for each PZT element. Table 3 represents the four potential combinations of those values. Having a matching network made up of only inductors (Case 4) consumed too much space and was expensive. On the other hand, a matching network made up of only capacitors (Case 3) could not achieve a narrow enough bandwidth for the desired frequency. Case 1 configuration is a low pass filter and Case 2 configuration is a high pass filter. Both cases can be beneficial because a high pass filter will reduce the effects of unwanted DC drifts and a low pass filter will reduce the effects of harmonic distortion. Between Case 1 and Case 2 I selected Case 2 as the dominating matching network design because I had more size and price options for the inductors with lower values. The benefit of having multiple configurations to choose from was evident when I ran into a logistical issue with the PZT ID A3. I ran out of inductors at the value of $75\mu\text{H}$. Instead of ordering more inductors, I improvised by designing that specific matching network using the Case 1 configuration values with a 1.2 nF shunt capacitor and an $82\mu\text{H}$ series inductor. The efficiency of the matching network was not compromised by the switch from Case 1 to Case 2.

I consulted with Jack Williams, Chris Quinkert, and Jay Shah about the desired parameters for my inductors and capacitors. I wanted a high voltage and current rating for my reactive components and a higher tolerance to conserve the matching network benefits. Final parameters were set based on prices. I chose a tolerance of 5% for the capacitors and a tolerance of 20% for the inductors. The price and size of inductors increased with the tolerance, so a 20% tolerance was selected as a compromise between price and specificity. The inductors were the largest component on the board, with the largest being $8\text{ mm} \times 8\text{ mm} \times 4\text{ mm}$, so I chose the rest of the components for the matching and amplification network to be less than this package size. The total amount spent on the SMD components is listed in Table 6. A full breakdown of the unit prices for the SMD components can be found in Table S4 and Table S5. With Christian's code I was able confirm that my purchased component values achieved a matching network that was within ± 5 kHz of the target resonance frequency. Figure 14 is a graphical representation of the efficiency of one of the PZT element's matching network with respect to the target resonance frequency. I further characterized my matching network by using SWR and Γ to calculate the percentage of power being delivered from the source to the load (Table 9). All of my matching

networks were calculated to have a power transfer efficiency of at least 99%. All of the values used to fully characterize the matching networks are reported in Table S1.

4.5. Prototyping Design Considerations

In all, I fabricated two prototypes before the final third prototype was made. Throughout the trial and error process of building each prototype, I developed design and fabrication methods that proved invaluable for the success of the final iteration, referenced as the LIFU device. The results from these two prototypes are presented in the Supplementary portion of this document.

4.5.1. Prototype I

The first prototype I built contained PZT elements that had a diameter and thickness of 7.0 mm x 0.03 mm and operated at a resonance frequency of 300 kHz. These elements are offered with or without wires. The pre-wired elements had wires jutting out from the side of the element as shown in Figure 23 which was not ideal for building a phased array with the elements closely packed. Therefore, with spatial considerations in mind, I decided to purchase the elements without wires and put them on myself. According to the STEMiNC website, wires could be manually attached under precise soldering conditions: using at least 2% silver content solder material and soldering within 2 seconds at a temperature of 250 to 270°C (STEMiNC). However, my attempts to follow the listed instructions resulted in failure. Alternately, I used a soldering iron to quickly tap the solder and set it. Although this worked, the heat had drastically changed the PZT element's original impedance. I then purchased silver conductive epoxy adhesive that would set without the need for heat (MG Chemicals). Unfortunately, this epoxy had a long curing time, making it difficult to setup the wires, epoxy, and element to sit overnight. Even when it was successful, the wires easily detached and also took part of the electrode with it. While the impedance of the PZTs did not change as drastically as when heat was applied, user-handling of the PZT elements was not feasible for constructing a phased array since the wires could not handle any strain.

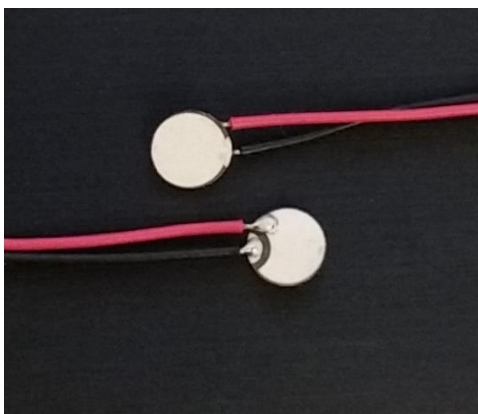


Figure 23: Front and back of PZT element showing wires attached by the company

It was important to find any other fabrication issues throughout the process, so for the first prototype with the larger PZT elements and wires I soldered on I moved forward with constructing the device. I next encountered troubles while creating the silicone backing layer. I hand mixed the silicone and poured it into the back of the device. The poor mixing resulted in uncured silicone as well as large air pockets due to the material being too viscous to flow into tighter areas. This prototype did not initially have a matching layer of epoxy. I was unsure of how to proceed with achieving a specific concave thickness of epoxy. Instead, a protective covering of thin latex was placed over the transducer head to protect the PZTs and their electrical connections during testing in water. However, the PZT elements began to turn brown. The difference in color can be seen in Figure 24. After consulting with the company, I learned that this phenomenon was due to oxidation of the silver electrode surface. They said this did not affect the performance. Once more of the PZT elements began to discolor, I applied an arbitrary layer of epoxy over the PZTs to quickly protect them from the environment. I knew the importance of protecting the electrical connections from the water when testing, but I had not accounted for oxidation.

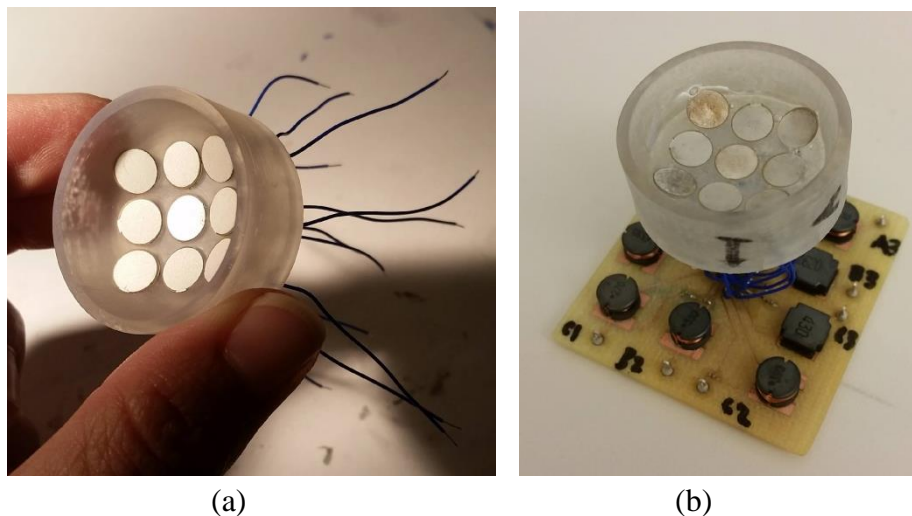


Figure 24: Prototype I. (a) Design of transducer without protective epoxy layer. (b) Finished prototype with protective epoxy layer and matching network.

The matching network was fabricated based on values I recorded from the PZTs after wires were soldered to them, but before they were secured into the transducer head. Instead of treating the transducer as a phased array, I instead had a pin out for each PZT element and its respective matching network. I wanted to evaluate how each PZT performed. The recorded peak to peak voltage amplitude values were very weak. This poor signal was likely due to two reasons: damage via heat exposure and having air as the medium for the ultrasound to travel from the PZTs to the hydrophone. Although not all the PZTs worked, the ones that did work emitted signals that were stronger with the epoxy layer than without. The values I recorded can be found in the Table S6. Overall, prototype I provided me with valuable insight on the nuances of the fabrication process.

4.5.2. Prototype II

The second prototype was constructed using disc-shaped PZT elements with a diameter and thickness of 5.0 mm x 0.4 mm and a resonance frequency of 450 kHz. Additionally, for this prototype, I ordered the pre-wired PZT elements. Upon the arrival of the PZTs, I made sure to always handle them with gloves on and kept them in individual bags, only to be taken out for measurement or fabrication. This was to minimize oxidation of the PZT elements, even though the company assured me the oxidation would not affect performance. I then measured their impedance values. Unfortunately, all of the pre-made PZT elements that arrived within the same batch of ten had varying Z and theta values. The variability was even greater between the PZT elements that had wires attached by the company. This variability was expected and can be attributed to impurities in the raw material that cause changes in PZT properties during the sintering process [39]. Within the same lot the elastic properties can vary by 5%, piezoelectric properties can vary by 10% and the dielectric properties can vary by 20% [39]. The variability between the PZT elements with wires attached was compounded by the additional heat this batch was exposed to during the soldering process. However, the differences within the PZT elements would not be an issue for the overall phased array design because the matching networks compensated for the varying impedances. Furthermore, the large difference in Z and theta values between the PZTs seen in Table 7 did not yield a large difference in matching network values. Referencing Table 9, there is little difference between the inductor and capacitor values, which logistically is ideal when ordering components.

Since the PZT elements behaved sensitively to various fabrication processes, I decided to measure the PZT elements' impedances after the transducer was fully constructed with the backing and matching layers. Although heat was not applied at any point in the construction process, the material properties of the PZT can still be affected. Specifically, silicone and epoxy have shown to have a capacitive effect on the material properties of the PZT, which can be attributed to the PZT being pre-loaded by polymer shrinkage. This was determined after discussion with the company about the change in the PZT impedances. The equivalent circuit for the PZT element values went from being inductive to capacitive, which changed how the matching network was calculated for. Specifically, the phase of the PZTs changed from positive to negative, but the resonance frequency of each PZT remained within ± 10 kHz of the manufacture-specified resonance frequency. After constructing the transducer head, I waited a few days before measuring the PZT elements' impedances again to see if there was a significant drift over time. Based on the new values I collected, none of the PZT elements' matching networks needed to be changed. A comparison of the change in a PZT's impedance and calculated matching network values upon arrival, immediately set in the transducer, and a week after being set in the transducer is provided in Table S7. These results showed the importance of knowing when to measure the PZT impedance for calculations that pertain to the matching network.

For the backing and matching layers I consulted with Dan Pederson and Jesse Somann on how to create the negative mold putty and how to properly mix the silicone and epoxy. They suggested I use mixing tips to ensure equal parts were mixed, no air was introduced into the material, and detailed application of the material due to the tip. It was especially important for the epoxy to have no air bubbles because they would impede the path of the ultrasound.

However, with the addition of the wires sticking straight out from the PZT elements, I was unable to bend the wires back to snugly fit the PZTs into the slots on the transducer head. To avoid wasting the 3D-printed concave disc, I used a Dremel to grind the edges of the component, making notches that the wires could freely jut out from. The modified transducer with the PZT element wires is shown in Figure 25.

When creating the epoxy matching layer, I ran into more issues when I tried placing my mold putty negative over the top of the transducer. When testing my fabrication procedure for the matching layer, the result shown in Figure 6, I did not account for wires coming out of the sides of the transducer. The wires were blocking the negative from achieving the specific fit necessary for the 0.8 mm thickness. I tried cutting away as much of the side of the mold putty that used to hug the side of the transducer for a secure fit. However, the wires proved too big of an issue and, upon removal of the negative, no epoxy set in the center portion of the transducer. I went back and manually applied epoxy to fill in the large air bubble region. At the end of the process there was an epoxy layer over the PZT elements, but it was much thicker than the desired quarter wavelength thickness.

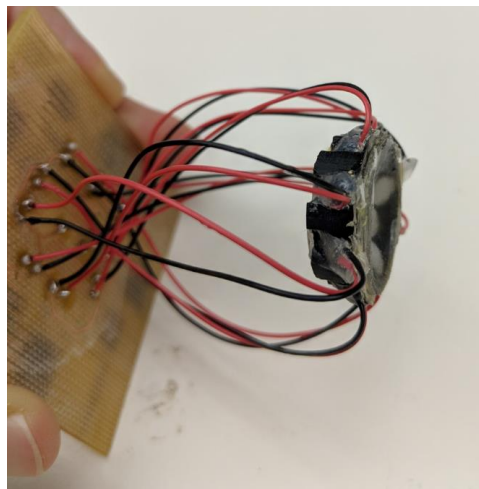


Figure 25: Prototype II and Dremel job

Moving forward with testing, I used a signal generator with an attached gain of 29 dB. I set it at 450 kHz and varied the location and amplitude of the hydrophone. At 10 mm away from the transducer edge with the signal generator set at 0 dBm I was able to pick up a signal. This confirmed that I was on the right track for achieving my design goals.

4.5.3. Prototype III

For the final design, I updated the 3D printed concave disc to have notches to compensate for the wires (Figure 4). Kevin Buno helped me with redesigning and printing the transducer with notches and molds used to create an updated negative mold putty component. I cut notches out of my negative mold putty to accommodate the wires and avoid air bubbles from a loose fit. The evolution of the negative mold putty is shown in Figure 26. I had no issues with applying or with setting the silicone and epoxy due to the use of mixing tips. The matching network was based on the final PZT element impedance measurements once they were fully incorporated into the transducer.



Figure 26: Mold Putty Negatives

The new addition to this prototype was the amplification network. I consulted a lot with Jack Williams, Chris Quinkert, and Jay Shah for this portion of the project. They helped me generate a list of search parameters to use when navigating Digi-Key. I wanted a SMD RF power amplifier that could operate in a low frequency range. SMD RF amplifiers on Digi-Key can cost hundreds to thousands of dollars. I was able to narrow my search further by incorporating my cost considerations into the equation. From there I chose the component with the highest gain and the least amount of additional components for the application circuit as size was a concern. The current draw from the 5 volt power source ranged from 0.5 A to 0.6 A. The device consumed 2.5 W to 3.0 W of power. It was difficult to set a specification for this portion of the design, but this overall power consumption was less than the power consumption of single active elements in HIFU designs [51], [74], [75], [77]–[79].

4.6. Size and Cost Considerations

Important design specifications for the LIFU device were the consolidation of the external networks and the overall size of the device. The final PCB board with the matching network on one side and the amplification network on the other was 50 mm x 57 mm. With the heat sink and transducer attached the length of the device was 76 mm. Images of the final LIFU device are shown in Figure 12. For a powerful comparison between the LIFU device and the H-115 system, I photographed them together in Figure 13. Both devices are pictured with their respective transducers, matching networks, and amplification networks. A 6 inch ruler was included in the picture for reference. The design specification for a small LIFU device was met.

Another priority for the LIFU device was the price. Again, a comparison between the two systems was based on the transducer, matching network, and amplifier. The H-115 transducer and matching network together cost \$4,250 (Table 5). The coupling cone, which needs to be paired with a stereotactic frame for precision focusing, costs \$685. The amplifier which was borrowed from Dr. Hugh Lee's lab costs \$4,900. The total cost for this system comes close to \$10,000. Even with the 5% academic discount offered by many of these companies, this is a high price to overcome without a grant. Systems like this one are also not customizable. The signal input and amplitude can be varied. However, the diameter and resonance frequency of the PZT element and the frequency range of the amplifier are set.

The total cost for the LIFU device was \$232.84, while the in-house total cost was \$80.94 (Table 6). This distinction was made because some of the materials were already available in the CID lab. These materials, such as the \$100 silicone, can easily be substituted for cheaper alternatives. For example, I was able to find a silicone of similar properties available in a 400 mL cartridge for \$20.00 (Smooth-On). CID and Purdue University's biomedical engineering department also had rapid prototyping tools available for student use, such as the 3D printer and milling machine. Both of these processes can be easily outsourced at a reasonable price. Regardless of these stipulations, the cost to build and customize the LIFU device is achievable for any research group. The design specification for an affordable LIFU device was met.

4.7. Intensity Considerations

When I characterized my device I varied the amplitude and location. Figure 15 shows an 8 mm x 20 mm 2D intensity field calculated from the data collected by the hydrophone. I used a function generator set at a 450 kHz sine wave and a - 3 dBm amplitude. I started my measurements at the center of the transducer and moved by 2 mm increments to 20 mm in the z axis. I moved 4 mm in both directions from the center of the transducer in the x axis. Closest to the transducer face there is an increased intensity due to the proximity to the PZT elements. The intensity had a slight increase at 4 mm and then reached peak intensity at a further distance away from the transducer, representing the focal region. A similar trend and location for the focal region were simulated in MATLAB in Figure 3. This was a success because the trends measured accurately characterized the general expected shape for an FUS beam. At certain parameters the beam will achieve a focused region some distance away from the transducer face. Furthermore, the measured focal region location matches the simulated focal region location from the transducer edge. This indicates that I was able to mimic the shape of a curved PZT element with a geometrically focused phased array to achieve my design specification for the focal length. It is also important to note the need for deionized water and a rubber lined container. The deionized water is safer to work with because of its lack of conductivity. The rubber lined container decreased the likelihood of echoes effecting the hydrophone measurements.

To investigate the future of beam steering for future iterations I disconnected three of the PZT channels. The FUS beam was created from constructive and destructive ultrasound waves

and when I introduced an imbalance in the transducer the focal region shifted by 8 mm (Figure 16). I created a shifted 10 mm x 20 mm 2D intensity map using the same frequency and amplitude parameters I used for the center focused intensity map. The recorded focal region was 1 mm x 1 mm and occurred between 10 mm and 14 mm. Beam steering is typically achieved using time delays to influence the location, size, and intensity of the focal region.

To further characterize the center focused focal region identified in Figure 15, I selected a region of interest and varied the amplitude from -6 dBm to 9 dBm. The region of interest occurred 10 mm to 12 mm from the center of the transducer and is 2 mm x 3 mm. I chose -6 dBm as the minimum amplitude because no focal region appeared at lower amplitudes. I chose 9 dBm as the maximum amplitude because the amplifiers have a maximum RF input power of 12 dBm. It is not advised to operate near or at the maximum limit. Based on the shape and location of the FUS beam, I selected -3 dBm as the amplitude for my animal studies. I wanted to ensure that the vagus was receiving therapy, so I chose a larger focal region than the other focal regions of 0.5 mm x 1 mm achieved at the varying amplitudes (Figure 17). At this amplitude the focal region is about 1 mm x 4 mm occurring between 10 mm and 12 mm from the edge of the transducer. The instantaneous intensity at the focal region is 38 mW/cm².

The potential issue with my FUS beam is that I did not pulse the signal. When testing prototype II I used a signal generator that was set to output a 450 kHz sine wave at varying amplitudes represented in dBm. When characterizing and comparing my device I used my Prototype II results as a point of reference and in doing so mimicked those parameters with the function generator for the rest of my work. In terms of customization, a greater instantaneous intensity can be achieved because the maximum input amplitude that the amplifiers can take is 12 dBm. Researchers can easily calculate a desired I_{SPTA} from the instantaneous intensity and apply it to their experiments. I also chose to not go above -3 dBm because I wanted to achieve a therapeutic response in the animal study, while balancing device longevity and power consumption concerns. Researchers in LIFU studies used pulsed signals to mechanically stimulate the nerve, but the parameters in terms of frequency, intensity, and pulsed signal vary across the board [68], [87], [89]–[93]. The parameters I selected may not be traditional, but I was able to induce a therapeutic response in the animal study.

4.8. Surgical and Statistical Considerations

4.8.1. Animal Exclusion Criteria

A total of twelve rats received VNS therapy and are designated with the label FUS. Based on the cost of rats, housing fee, time and resources twelve rats was the maximum amount of experiments my team and I could perform. Four rats were removed from the analysis based on events I recorded in their surgical logs. The LPS was not premade for FUSx002 – FUSx005. We were using the last of the LPS bought for other experiments. The manual method for making the

5mg/mL LPS solution involved weighing LPS, adding the saline, and then sonicating for 30 minutes before injection. The issue with this method was that the LPS was very light, making it difficult to measure out small quantities on the scale of milligrams. These difficulties contributed to the issue of not making enough LPS due to time constraints. FUSx003 was removed because I did not make enough LPS that day and had to go remake it, but since I was behind schedule (for blood collections) the LPS was not sonicated for the full 30 minutes. Once the first blood collection is taken the timeline is strict. If a time point is missed the experiment cannot be completed. For FUSx010, when the LPS was injected, a liquid bubble formed at the injection site. This is indicative of a failed IP injection and this event did not occur for any of the other animals. For FUSx007, oxygen was not being supplied to the correct nosecone. This was corrected when the heart rate dropped. Then, between the fifth and sixth blood collection, the rat stopped breathing twice and had to be revived. I threw out FUSx012, because the breathing was elevated (340 – 380 bpm) throughout the experiment. It was observed that the rat was not responding well to the anesthesia. We chose to exclude these animals from the analysis based on the surgical log recordings and past experience with animal work involving ket/xyl and LPS.

4.8.2. Analysis of TNF- α Concentration

LPS was first injected at time point “0 minutes.” No blood was taken at this time point, so an elevated response is not visible until time point “30 minutes.” The average concentration of TNF- α for the control data and the FUS data was plotted in Figure 18. We wanted to determine the peak of the TNF- α concentration and analyze at that specific time point because this is where the effect of the therapy will be the most evident and effective. The average control data showed a peak value at time point “90 minutes.” The error bars also need to be considered. There is no overlap of the error bars at time point “90 minutes.” At later time points of “120 minutes” and “150 minutes,” the difference between replicates dramatically increased. This observed variability was due to these later time points being outside of the linear region on the calibration curve used for extrapolating cytokine concentrations. In flow cytometry, measurements are less reliable outside of the linear region. The average difference in replicates at time point “90 minutes” was approximately 100 pg/mL with a maximum value of 380 pg/mL. The average difference in replicates at the later time points ranged from 400 to 500 pg/mL with a maximum value of 2,300 pg/mL. For time point “150 minutes” for uRx023 the average difference between the two replicates was 7,400 pg/mL. This data point was a clear outlier and was removed from the data.

To further support evaluating at time point “90 minutes” we conducted a Cohen’s h analysis. We used Cohen’s h to measure the difference between the two proportions and to determine if the difference was meaningful. Cytokine data for IL-6, IL-10 and TNF- α was available for all of the FUS rats and most of the control rats. IL-10 data was missing for two of the controls. We normalized the data based on the total proportion of cytokines measured at each time point. We then solved for the Gaussian distributed center log ratio for each cytokine. The average for the control data and FUS data were plotted against each other in Figure 19. For a

Cohen's h analysis a meaningful difference is represented as small (greater than 0.2), medium (greater than 0.5), and large (greater than 0.8). The meaningful differences recorded occurred at time points "60 minutes" and "90 minutes" with a difference between the control and FUS data of 0.63 and 0.47, respectively (Table 10). The error bars also do not overlap at time point "90 minutes".

We next performed a two-sample t -test with an $\alpha = 0.05$ between the controls and the rats that received the LIFU device therapy at time point "90 minutes." The P value was 0.0845, which meant that the results were not statistically significantly different. Reasons for no response from the rats could be that the transducer was not placed correctly and these rats did not receive the full therapy. Another reason could be that these rats had an inflammation response to the LPS that the therapy could not overcome.

The results of this type experiment will either indicate that the rat did or did not respond to the therapy. If the rat does respond to the therapy there are varying degrees to how the $\text{TNF-}\alpha$ concentration is affected. When the rat does not respond to the therapy these values mimic control values and will heavily influence the overall data. Although the results were not statistically significantly different, there is an observable trend in Figure 20. When comparing individual rats to the average concentration of the controls there appears to be a therapeutic response. Comparing each rat against the control, five of the eight rats appeared to respond to the therapy.

4.8.3. Studentized Residuals

It was suggested by Hakeem to conduct an evaluation of the studentized residuals to identify which of the rats that did not respond to the therapy. Residuals represent the error between the predicted value and the actual values. The standard error between each of the residuals will vary, so the residual values are divided by an estimate of its standard deviation. This is called the studentized residuals and these values can be used to detect outliers in the data [100],[101]. Each data point will have a certain amount of leverage on the overall data set. The average leverage of a data set is represented as 1. The general rule is to double this value and use that as a cutoff threshold for data points that have a large amount of leverage on the data set. When the studentized residual value is positive it is an overestimate and when it is negative it is an underestimate. Another important measurement is the Cook's Distance (Cook's D), which represents a cutoff threshold for outliers [100]. Another general standard is to use 0.5 or 1 as a cutoff. However, when there are minimal observations another option is to set the cutoff at the value of four divided by the number of observations.

The first pass of studentized residual calculations, shown in Table S2, yielded an overestimate for FUSx005 at 2.08. For FUSx005 its $\text{TNF-}\alpha$ concentration at time point "90 minutes" is greater than four out of the five controls (Figure 20). This value meets the ± 2.0 threshold for removal and was one of the FUS data sets identified worth investigating based on

domain knowledge. Domain knowledge is in reference to us knowing that some of the rats did not respond to the therapy and will instead mimic control data. Looking at the Cook's D and leverage plots in Figure S1, we determined that this FUS data point had considerable influence on the overall data. We removed FUSx005 and then performed a two-sample t-test on the remaining control and FUS data. The P value was 0.0274. The results are statistically significantly different.

We then recalculated the studentized residuals and also identified FUSx009, with a value of 2.3, as a rat that did not respond to the therapy (Table S3). We performed another two-sample t-test on the remaining control data and FUS data. The P value was 0.0062. The results remained statistically significantly different. All of the diagnostic plots for each calculation are located in the supplementary section (Figure S1, Figure S2, Figure S3). No more studentized residual calculations were conducted because no more FUS data points were above cutoff thresholds. The shape of the QQ-plots and histogram plots further supports the removal of the two FUS data points. The final histogram plot has a clear normal distribution, whereas the preceding two did not. After removing the data points that were having a significant effect on the overall data, the diagnostic plots convey a constant variance and normal distribution, which means that our assumptions and inferences are valid (Figure S3). When the therapy was determined effective; its effect was shown to be statistically significantly different from the controls. This is motivation enough to further investigate the effect of the LIFU device on the modulation of cytokines and to fine-tune the stimulation parameters used.

Overall, it is well known that there is inherent variability in animal studies. As such, it was important to conduct many experiments to account for physiological variables. It would have been interesting to apply other types of stimulation parameters; however I was unable to do this due to the time and resources required for conducting animal studies and processing data. Instead, I used the time and resources I had and prioritized statistical power by increasing the number of replicates.

4.9. Future Considerations

Future work for this project would be to continue to consolidate and incorporate the larger aspects of the setup. I was able to eliminate the need for an expensive amplifier. However, there is always room for improvement in the amplification stage. Biomedical technologies prioritize power transfer efficiency and take advantage of this aspect by sacrificing linearity, which is usually important in circuit design [63]. Non-linear amplifiers, such as Class D and E amplifiers, use two transistors that operate as switches to handle the output stage when no signal is present. This class of amplifiers also has very low power dissipation and high power capabilities [63]. However, many of the Class D amplifiers are for audio usage and have optimal efficiency when their load impedance matches the standard impedance of speakers, which is typically 4, 8, or 16 ohms [102]. The risk of using this type of amplifier in my system is because it consists of reactive components. Modern technology employs resistive components, such as transistors, so impedance mismatching is not as detrimental because the systems are more robust and can handle power reflection and heat generation [103]. Christian and I had looked into building our own amplifiers, but decided purchasing an off-the-shelf product was best for this prototype, as the focus of the project was LIFU and not amplifier design. For the future of this project I want the efficiency of the amplification stage to be further explored.

The next step would be to electronically steer the FUS beam and focal region. Instead of manually disconnecting channels, a field programmable gate arrays (FPGAs) could be incorporated onto the PCB board that would create the desired time delays associated with a specific focal distance [63]. The FOCUS MATLAB code I used to geometrically calculate the ROC I needed for my transducer also has the capability to calculate those phase values.

Future animal studies would involve applying a variety of intensities to the vagus nerve. It would be interesting to investigate and characterize the bimodal effect of excitation and suppression through signal parameter variations. Another aspect of the animal study that can be expanded on is removing physiological based LPS variability in the study. For example, for the first phase of the experiment the rat would be injected with LPS and have blood collections taken at the same time points. The rat would then be given time to recover and for the second phase of the experiment the LIFU device therapy would be applied. The results from the first phase of the experiment could be compared against the results from the second phase of the experiment. This would eliminate the issues that pertain to the differing inflammatory responses to LPS between rats that have been measured. The long term goal of this application for animal studies would be incorporating ultrasound imaging to find the vagus and based on that location use the LIFU device to stimulate. With the combined use of ultrasound imaging, the noninvasive capability of the LIFU device could truly be tested in chronic animal studies.

5. CONCLUSIONS

Research has shown a correlation between depression and the inflammatory response. VNS is a form of therapy that can decrease the inflammatory response through the modulation of cytokines. Two forms of stimulation that are commonly investigated are electrical and LIFU. Cuffing the nerve to achieve electrical stimulation has various side effects, such as damaging the nerve. The solution is to use FUS to stimulate the nerve without touching it. However, the price range for FUS systems is in the thousands. In response to the lack of affordable and customizable FUS systems, I designed my own LIFU device. My main design considerations were for cost and size. The final LIFU device design is composed of a transducer, matching network, and amplification network.

Unable to find a curved PZT element, which most LIFU studies employ in their research, I constructed my own geometrically focused phased array. I applied my own backing and $\lambda/4$ thickness matching layer to create the transducer. I incorporated matching networks into the design that have a power transfer efficiency of at least 99%. An amplification network was built in to eliminate the need for an industrial sized amplifier that can cost thousands of dollars. I presented a detailed outline for the fabrication process and a list of off the shelf materials used. With the resources available in my lab, I was able to build a 50 mm x 57 mm x 76 mm device for \$81.00. The LIFU device consumes 2.5 W to 3 W of power and can achieve an instantaneous intensity of up to 350 mW/cm^2 at 10 mm to 12 mm away from the transducer. I also showed that this device is capable of beam steering by manually disconnecting channels to shift the location of the focal region by 8 mm.

I conducted an animal study investigating the therapeutic effect of my LIFU device on a rat model of the inflammation response. The concentration of the pro-inflammatory cytokine, TNF- α , was collected and analyzed. Based on a two-sample t-test with an $\alpha = 0.05$ there was no statistical significance between the controls and the treatment group. However, it was observed that five rats out of the eight rats had lowered concentrations at the time point of analysis than the control. I worked with a statistics consultant to identify data points with a large leverage. Based on studentized residuals, we removed two FUS rats that did not respond to therapy. When the therapy was determined effective; its effect was shown to be statistically significantly different from the controls. The results indicate that there is merit to this form of therapy. Future work will involve more animal work and applying different stimulation parameters.

As biomedical equipment becomes larger and more advanced, increasing costs become a major barrier to research. I have created a device and a fabrication process that is repeatable and customizable for any research group. The size of the LIFU device is a step in the direction towards wearable technology. The low cost of the LIFU device can be used to expand research in the field of neuromodulation.

REFERENCES

- [1] “WHO | Depression,” *WHO*, 2017.
- [2] P. E. Greenberg, C. T. Pike, and R. C. Kessler, “The Economic Burden of Adults With Major Depressive Disorder in the United States (2005 and 2010),” *Orig. Res. J Clin Psychiatry J Clin Psychiatry*, vol. 15576, no. 7622, pp. 155–162, 2015.
- [3] P. L. Delgado, “Depression: the case for a monoamine deficiency,” *J. Clin. Psychiatry*, vol. 61 Suppl 6, pp. 7–11, 2000.
- [4] Y. Dowlati *et al.*, “A Meta-Analysis of Cytokines in Major Depression,” *Biol. Psychiatry*, vol. 67, no. 5, pp. 446–457, 2010.
- [5] J. H. Meyer *et al.*, “Elevated Monoamine Oxidase A Levels in the Brain,” *Arch. Gen. Psychiatry*, vol. 63, no. 11, p. 1209, Nov. 2006.
- [6] Mayo Clinic, “Selective serotonin reuptake inhibitors (SSRIs) - Mayo Clinic.” [Online]. Available: <https://www.mayoclinic.org/diseases-conditions/depression/in-depth/ssris/art-20044825>. [Accessed: 15-Nov-2017].
- [7] A. H. Miller and C. L. Raison, “Imperative To Modern Treatment Target,” vol. 16, no. 1, pp. 22–34, 2017.
- [8] K. Aschbacher, E. Epel, O. M. Wolkowitz, A. A. Prather, E. Puterman, and F. S. Dhabhar, “Maintenance of a positive outlook during acute stress protects against pro-inflammatory reactivity and future depressive symptoms,” *Brain. Behav. Immun.*, vol. 26, no. 2, pp. 346–352, 2012.
- [9] P. J. Watson and P. W. Andrews, “Toward a revised evolutionary adaptationist analysis of depression: The social navigation hypothesis,” *J. Affect. Disord.*, vol. 72, no. 1, pp. 1–14, 2002.
- [10] A. Bierhaus *et al.*, “A mechanism converting psychosocial stress into mononuclear cell activation,” *Proc. Natl. Acad. Sci.*, vol. 100, no. 4, pp. 1920–1925, 2003.
- [11] K. S. Al-Harbi, “Treatment-resistant depression: therapeutic trends, challenges, and future directions,” *Patient Prefer. Adherence*, vol. 6, pp. 369–88, 2012.
- [12] M. Fava, “Diagnosis and definition of treatment-resistant depression,” *Biological Psychiatry*, vol. 53, no. 8, pp. 649–659, 2003.
- [13] M. P. Ward and P. P. Irazoqui, “Evolving refractory major depressive disorder diagnostic and treatment paradigms: toward closed-loop therapeutics,” *Front. Neuroeng.*, vol. 3, p. 7, 2010.
- [14] A. H. Miller, E. Haroon, C. L. Raison, and J. C. Felger, “Cytokine targets in the brain: impact on neurotransmitters and neurocircuits,” *Depress. Anxiety*, vol. 30, no. 4, pp. 297–306, 2013.
- [15] V. Michopoulos *et al.*, “Association of CRP genetic variation and CRP level with elevated PTSD symptoms and physiological responses in a civilian population with high levels of trauma,” *Am. J. Psychiatry*, vol. 172, no. 4, pp. 353–362, 2015.

- [16] L. S. M. Eurelings, E. Richard, P. Eikelenboom, W. A. van Gool, and E. P. M. van Charante, "Low-grade inflammation differentiates between symptoms of apathy and depression in community-dwelling older individuals," *Int. psychogeriatrics*, vol. 27, no. 4, pp. 639–647, 2015.
- [17] A. Cattaneo *et al.*, "Candidate genes expression profile associated with antidepressants response in the GENDEP study: differentiating between baseline 'predictors' and longitudinal 'targets,'" *Neuropsychopharmacology*, vol. 38, no. 3, pp. 377–385, 2013.
- [18] G. M. Slavich and M. R. Irwin, "From stress to inflammation and major depressive disorder: A social signal transduction theory of depression.," *Psychol. Bull.*, vol. 140, no. 3, p. 774, 2014.
- [19] S. Tying *et al.*, "Etanercept and clinical outcomes, fatigue, and depression in psoriasis: double-blind placebo-controlled randomised phase III trial," *Lancet*, vol. 367, no. 9504, pp. 29–35, 2006.
- [20] O. Köhler *et al.*, "Effect of anti-inflammatory treatment on depression, depressive symptoms, and adverse effects: a systematic review and meta-analysis of randomized clinical trials," *JAMA psychiatry*, vol. 71, no. 12, pp. 1381–1391, 2014.
- [21] R. H. Howland, "New Developments With VNS Therapy," *J. Psychosoc. Nurs.*, vol. 182, no. 3, pp. 175–182, 1976.
- [22] A. H. Miller, V. Maletic, and C. L. Raison, "Inflammation and its discontents: the role of cytokines in the pathophysiology of major depression," *Biol. Psychiatry*, vol. 65, no. 9, pp. 732–741, 2009.
- [23] P. Brambilla *et al.*, "Increased M1/decreased M2 signature and signs of Th1/Th2 shift in chronic patients with bipolar disorder, but not in those with schizophrenia," *Transl. Psychiatry*, vol. 4, no. 7, p. e406, 2014.
- [24] A. Drago, C. Crisafulli, M. Calabrò, and A. Serretti, "Enrichment pathway analysis. The inflammatory genetic background in bipolar disorder," *J. Affect. Disord.*, vol. 179, pp. 88–94, 2015.
- [25] M. Maes, "Evidence for an immune response in major depression: a review and hypothesis," *Prog. Neuro-Psychopharmacology Biol. Psychiatry*, vol. 19, no. 1, pp. 11–38, 1995.
- [26] H. Yuan and S. D. Silberstein, "Vagus Nerve and Vagus Nerve Stimulation, a Comprehensive Review: Part III," *Headache*, vol. 56, no. 3, pp. 479–490, 2016.
- [27] K. J. Tracey, "Reflex control of immunity," *Nat. Rev. Immunol.*, vol. 9, no. 6, pp. 418–428, 2009.
- [28] S. C. Schachter and C. B. Saper, "Vagus nerve stimulation," *Epilepsia*, vol. 39, no. 7, pp. 677–686, 1998.
- [29] Bronte, "NIH Public Access," vol. 39, no. 5, pp. 213–223, 2015.
- [30] C. Galanos and M. A. Freudenberg, "Bacterial endotoxins: biological properties and mechanisms of action," *Mediators Inflamm.*, vol. 2, no. 7, pp. S11–S16, 1993.
- [31] F. A. Koopman *et al.*, "Vagus nerve stimulation inhibits cytokine production and attenuates disease severity in rheumatoid arthritis," *Proc. Natl. Acad. Sci.*, vol. 113, no. 29, pp. 8284–8289, 2016.

- [32] U. Andersson and K. J. Tracey, "Neural reflexes in inflammation and immunity," *J. Exp. Med.*, vol. 209, no. 6, pp. 1057–1068, 2012.
- [33] J. M. Huston *et al.*, "Splenectomy inactivates the cholinergic antiinflammatory pathway during lethal endotoxemia and polymicrobial sepsis," *J. Exp. Med.*, vol. 203, no. 7, pp. 1623–1628, 2006.
- [34] J. Meregnani *et al.*, "Anti-inflammatory effect of vagus nerve stimulation in a rat model of inflammatory bowel disease," *Auton. Neurosci.*, vol. 160, no. 1, pp. 82–89, 2011.
- [35] U. Andersson and K. J. Tracey, "Reflex principles of immunological homeostasis," *Annu. Rev. Immunol.*, vol. 30, pp. 313–335, 2012.
- [36] L. V Borovikova *et al.*, "Vagus nerve stimulation attenuates the systemic inflammatory response to endotoxin," *Nature*, vol. 405, no. 6785, pp. 458–462, 2000.
- [37] R. H. Howland, "Vagus Nerve Stimulation Robert," vol. 1, no. 2, pp. 64–73, 2015.
- [38] J. P. Somann *et al.*, "Chronic cuffing of cervical vagus nerve inhibits efferent fiber integrity in rat model."
- [39] T. L. Jordan and N. Langley, "Piezoelectric Ceramics Characterization," *Contract*, p. 23, 2001.
- [40] F. Kremkau, "Basic Physical Principles of Ultrasound."
- [41] A. Ng and J. Swanevelder, "Resolution in ultrasound imaging," *Contin. Educ. Anaesthesia, Crit. Care Pain*, vol. 11, no. 5, pp. 186–192, 2011.
- [42] Olympus, "ultrasonic transducer technical notes." .
- [43] G. R. ter H. Victoria Bull, "The Physics of Ultrasound," vol. 1, pp. 175–186, 2015.
- [44] K. T. Selvan and R. Janaswamy, "Fraunhofer and Fresnel Distances," no. June, pp. 12–15, 2017.
- [45] J. Stiles, "Chapter 5 – Impedance Matching and Tuning," pp. 3–5, 2009.
- [46] H. J. Gohari, "Focusing of ultrasound beams," pp. 1–102, 1997.
- [47] J. Jang and J. H. Chang, "Design and fabrication of double-focused ultrasound transducers to achieve tight focusing," *Sensors (Switzerland)*, vol. 16, no. 8, pp. 3–4, 2016.
- [48] F. Souris *et al.*, "Design, fabrication and characterization of a monolithic focusing piezoceramic transducer for an anisotropic material," *Rev. Sci. Instrum.*, vol. 85, no. 6, 2014.
- [49] J. Y. Zhang *et al.*, "Numerical and experimental investigation of kerf depth effect on high-frequency phased array transducer," *Ultrasonics*, vol. 52, no. 2, pp. 223–229, 2012.
- [50] L. F. Brown, "The effects of material selection for backing and wear protection/quarter-wave matching of piezoelectric polymer ultrasound transducers," *2000 IEEE Ultrason. Symp. Proceedings. An Int. Symp. (Cat. No.00CH37121)*, vol. 2, pp. 1029–1032, 2000.
- [51] H. Lee, D. Francischelli, and N. B. Smith, "Design of Focused Ultrasound Array for Non-Invasive Transesophageal Cardiac Ablation," pp. 51–53, 2010.
- [52] H. Guo, "NIH Public Access," *IEEE Eng. Med. Biol. Mag.*, pp. 1–17, 2008.

- [53] M. R. Draheim and W. Cao, "Finite element analysis on impedance matching layer thickness," *Appl. Ferroelectr. 1996. ISAF '96., Proc. Tenth IEEE Int. Symp.*, pp. 1015–1018, 1996.
- [54] Y. Lin and K. Grosh, "Topology optimization of the kerf fillings in linear phased arrays for therapy," *J. Acoust. Soc. Am.*, vol. 112, no. 5, p. 1968, 2002.
- [55] H. Li, Z. D. Deng, Y. Yuan, and T. J. Carlson, "Design parameters of a miniaturized piezoelectric underwater acoustic transmitter," *Sensors (Switzerland)*, vol. 12, no. 7, pp. 9098–9109, 2012.
- [56] M. G. S. Ali, "Analysis of broadband piezoelectric transducers by discrete time model," *Egypt. J. Sol*, vol. 23, no. 2, pp. 287–295, 2000.
- [57] M. Garcia-Rodriguez *et al.*, "Low cost matching network for ultrasonic transducers," *Phys. Procedia*, vol. 3, no. 1, pp. 1025–1031, 2010.
- [58] J. An, K. Song, S. Zhang, J. Yang, and P. Cao, "Design of a Broadband Electrical Impedance Matching Network for Piezoelectric Ultrasound Transducers Based on a Genetic Algorithm," *Sensors*, vol. 14, no. 4, pp. 6828–6843, 2014.
- [59] IEEE, *IEEE Standard on Piezoelectricity*. .
- [60] J. Kim, "Multi-Mode Shunt Damping of Piezoelectric Smart Panel for Noise Reduction," *Noise Vib. Worldw.*, vol. 37, no. 7, pp. 10–17, 2006.
- [61] JamproAntennas, "VSWR Return Loss Conversion Table." [Online]. Available: <http://www.jampro.com/document-library.html>. [Accessed: 05-Dec-2017].
- [62] MaximIntegrated, "Impedance Matching and the Smith Chart: The Fundamentals - Tutorial - Maxim." [Online]. Available: <https://www.maximintegrated.com/en/app-notes/index.mvp/id/742>. [Accessed: 05-Dec-2017].
- [63] M. M. El-Desouki and K. Hynynen, "Driving circuitry for focused ultrasound noninvasive surgery and drug delivery applications," *Sensors*, vol. 11, no. 1, pp. 539–556, 2011.
- [64] G. Fleury *et al.*, "Safety issues for HIFU transducer design," in *AIP Conference Proceedings*, 2005, vol. 754, no. 1, pp. 233–241.
- [65] J. T. Bushberg, *The essential physics of medical imaging*. Lippincott Williams & Wilkins, 2002.
- [66] P. Laugier and G. Haïat, "Bone quantitative ultrasound," *Bone Quant. Ultrasound*, pp. 1–468, 2011.
- [67] T. Reson, "Hydrophone_Intensity_Calculations." .
- [68] H. Baek, K. J. Pahk, and H. Kim, "A review of low-intensity focused ultrasound for neuromodulation," *Biomed. Eng. Lett.*, vol. 7, no. 2, pp. 135–142, 2017.
- [69] Sonic Concepts, "H- Ø64 H- Transducer Series Ø64 mm H- Ø64," vol. 1, no. 425.
- [70] Alkhorayef, "High-Intensity Focused Ultrasound (HIFU) in Localized Prostate Cancer Treatment," *Polish J. Radiol.*, vol. 80, pp. 131–141, 2015.
- [71] J. Barkin, "HIFU: Definitely ready for prime time," *Can. Urol. Assoc. J.*, vol. 5, no. 6, pp. 422–423, 2011.

- [72] "SonaCare." [Online]. Available: <http://sonacaremedical.com/index.php/about/company-history>.
- [73] G. T. Clement *et al.*, "Investigation of a large-area phased array for focused ultrasound surgery through the skull," 2000.
- [74] M. Wada *et al.*, "Design and evaluation of A3×21 Element 1.75 Dimensional tapered ultrasound phased array for the treatment of prostate disease," *Mater. Res. Innov.*, vol. 8, no. 2, pp. 121–124, 2004.
- [75] K. Y. Saleh and N. B. Smith, "A 63 element 1.75 dimensional ultrasound phased array for the treatment of benign prostatic hyperplasia," 2005.
- [76] Mingzhu Lu, Mingxi Wan, Feng Xu, Xiaodong Wang, and Hui Zhong, "Focused beam control for ultrasound surgery with spherical-section phased array: sound field calculation and genetic optimization algorithm," *IEEE Trans. Ultrason. Ferroelectr. Freq. Control*, vol. 52, no. 8, pp. 1270–1290, Aug. 2005.
- [77] X. Ji, J. Bai, G. Shen, and Y. Chen, "High-intensity focused ultrasound with large scale spherical phased array for the ablation of deep tumors," *J. Zhejiang Univ. Sci. B*, vol. 10, no. 9, pp. 639–47, Sep. 2009.
- [78] J. Liu, J. Foiret, D. N. Stephens, O. Le Baron, and K. W. Ferrara, "Development of a spherically focused phased array transducer for ultrasonic image-guided hyperthermia," *Phys. Med. Biol.*, vol. 61, no. 14, pp. 5275–5296, 2016.
- [79] Y. Zhou, L. Zhai, R. Simmons, and P. Zhong, "Measurement of high intensity focused ultrasound fields by a fiber optic probe hydrophone," *J. Acoust. Soc. Am.*, vol. 120, no. 2, pp. 676–685, 2006.
- [80] D. Dalecki, "Mechanical bioeffects of ultrasound," *Annu. Rev. Biomed. Eng.*, vol. 6, pp. 229–248, 2004.
- [81] F. Lizzi *et al.*, "Bioeffects considerations for the safety of diagnostic ultrasound," *J. ultrasound Med.*, vol. 7, no. 9 SUPPL., 1988.
- [82] M. J. Crocker, *Encyclopedia of acoustics*. John Wiley, 1997.
- [83] W. L. Nyborg, "Mechanisms for bioeffects of ultrasound relevant to therapeutic applications," in *Emerging Therapeutic Ultrasound*, World Scientific, 2006, pp. 5–66.
- [84] W. J. Fry and F. J. Fry, "Fundamental neurological research and human neurosurgery using intense ultrasound," *IRE Trans. Med. Electron.*, no. 3, pp. 166–181, 1960.
- [85] S. Madersbacher, M. Pedevilla, L. Vingers, M. Susani, and M. Marberger, "Effect of high-intensity focused ultrasound on human prostate cancer in vivo," *Cancer Res.*, vol. 55, no. 15, pp. 3346–3351, 1995.
- [86] E. Mehić, J. M. Xu, C. J. Caler, N. K. Coulson, C. T. Moritz, and P. D. Mourad, "Increased anatomical specificity of neuromodulation via modulated focused ultrasound," *PLoS One*, vol. 9, no. 2, 2014.
- [87] W. J. Tyler, Y. Tufail, M. Finsterwald, M. L. Tauchmann, E. J. Olson, and C. Majestic, "Remote excitation of neuronal circuits using low-intensity, low-frequency ultrasound," *PLoS One*, vol. 3, no. 10, p. e3511, 2008.

- [88] Mulgaonkar, "Explorations in targeting lifu for neuromodulation," 2012.
- [89] B.-K. Min *et al.*, "Focused ultrasound-mediated suppression of chemically-induced acute epileptic EEG activity.," *BMC Neurosci.*, vol. 12, p. 23, Mar. 2011.
- [90] H. Kim, S. J. Taghados, K. Fischer, L. S. Maeng, S. Park, and S. S. Yoo, "Noninvasive Transcranial Stimulation of Rat Abducens Nerve by Focused Ultrasound," *Ultrasound Med. Biol.*, vol. 38, no. 9, pp. 1568–1575, 2012.
- [91] D. . Xu, W. . Mao, and J. . Fang, "Is there a role of ultrasound stimulation in pain management? A literature review," *Int. J. Clin. Exp. Med.*, vol. 9, no. 5, pp. 7648–7654, 2016.
- [92] O. Naor, S. Krupa, and S. Shoham, "Ultrasonic neuromodulation," *J. Neural Eng.*, vol. 13, no. 3, p. 31003, 2016.
- [93] A. P. Mulgaonkar *et al.*, "Design of a minimally invasive low-frequency microtransducer for ultrasonic neuromodulation," *IEEE Int. Ultrason. Symp. IUS*, pp. 405–408, 2014.
- [94] F. J. Fry, "Precision high intensity focusing ultrasonic machines for surgery.," *Am. J. Phys. Med. Rehabil.*, vol. 37, no. 3, pp. 152–156, 1958.
- [95] H. Kim, "Suppression of EEG visual-evoked potentials in rats via neuromodulatory focused ultrasound," vol. 26, no. 5, pp. 213–223, 2015.
- [96] M. J. Guan and W. H. Liao, "On the equivalent circuit models of piezoelectric ceramics," *Ferroelectrics*, vol. 386, no. 1, pp. 77–87, 2009.
- [97] A. S. Korb, F. G. Shellock, M. S. Cohen, and A. Bystritsky, "Low-intensity focused ultrasound pulsation device used during magnetic resonance imaging: Evaluation of magnetic resonance imaging-related heating at 3 Tesla/128 MHz," *Neuromodulation*, vol. 17, no. 3, pp. 236–241, 2014.
- [98] Y. Younan, T. Deffieux, B. Larrat, M. Fink, M. Tanter, and J.-F. Aubry, "Influence of the pressure field distribution in transcranial ultrasonic neurostimulation," *Med. Phys.*, vol. 40, no. 8, p. 82902, 2013.
- [99] Dallapiazza, "Noninvasive neuromodulation and thalamic mapping with lifu," pp. 1–10, 2016.
- [100] R. D. Cook, "Detection of Influential Observation in Linear Regression," *JSTOR*, vol. 19, no. 1, 1977.
- [101] "Applied Linear Regression: Chapter 11 Diagnostics: Unusual and Influential Data: Outliers, Leverage, and Influence."
- [102] E. Hintzen, T. Vennemann, and W. Mathis, "Systematic design of output filters for audio class-D amplifiers via Simplified Real Frequency Technique," *Adv. Radio Sci*, vol. 12, pp. 49–52, 2014.
- [103] "Advanced Engineering: Impedance Matching."

SUPPLEMENTARY INFORMATION

Table S1: Calculated values for matching network efficiency

PZT	Complex Z_L	Z_L	SWR	Γ	Return Loss (dB)	Reflection Loss (dB)	Power Reflected (%)	Power Delivered (%)
A1	55.0139 + 6.848i	55.438	1.11	0.0516	25.750	0.012	0.266	99.734
A2	47.0180 + -1.818i	47.053	0.94	-0.0304	30.353	0.004	0.092	99.908
A3	51.5685 + -6.760i	52.010	1.04	0.0197	34.110	0.002	0.039	99.961
B1	45.5316 + 0.403i	45.533	0.91	-0.0468	26.604	0.010	0.219	99.781
B2	46.1425 + -9.727i	47.157	0.94	-0.0293	30.673	0.004	0.086	99.914
B3	52.7301 + 4.729i	52.942	1.06	0.0286	30.880	0.004	0.082	99.918
C1	49.5924 + 5.723i	49.922	1.00	-0.0008	62.099	0.000	0.000	100.000
C2	52.4808 + -3.987i	52.632	1.05	0.0256	31.820	0.003	0.066	99.934
C3	46.6006 + -4.976i	46.866	0.94	-0.0324	29.800	0.005	0.105	99.895

Table S2: SAS 94 generated studentized residual data for the FUS and control rats at the time point “90 minutes.” The data FUSx005 has the largest residual studentized value and is above +2.0.

The SAS System							
Obs	time	id	trt	repA	repB	avg	rstudent
1	90	uRx017	0	981.08	972.12	976.60	-1.06292
2	90	FUSx013	1	10.46	14.46	12.46	-1.05149
3	90	FUSx006	1	70.70	94.60	82.65	-0.95596
4	90	uRx023	0	1190.06	1133.36	1161.71	-0.80419
5	90	FUSx002	1	269.54	210.11	239.82	-0.75009
6	90	FUSx011	1	167.80	314.13	240.96	-0.74863
7	90	FUSx008	1	585.46	644.02	614.74	-0.28921
8	90	uRx016	0	2325.17	1384.42	1854.80	0.07485
9	90	uRx018	0	1916.41	2225.97	2071.19	0.34354
10	90	FUSx014	1	1273.92	1448.23	1361.08	0.60216
11	90	FUSx009	1	1997.43	1981.08	1989.26	1.46841
12	90	uRx025	0	2935.01	2877.23	2906.12	1.52081
13	90	FUSx005	1	2520.91	2143.23	2332.07	2.07663

Table S3: SAS 94 generated studentized residual data for the kept FUS and control rats at the time point “90 minutes.” The data for FUSx009 has the largest residual studentized value and is above +2.0.

The SAS System							
Obs	time	id	trt	repA	repB	avg	rstudent
1	90	uRx017	0	981.08	972.12	976.60	-1.23687
2	90	uRx023	0	1190.06	1133.36	1161.71	-0.92572
3	90	FUSx013	1	10.46	14.46	12.46	-0.89746
4	90	FUSx006	1	70.70	94.60	82.65	-0.79110
5	90	FUSx002	1	269.54	210.11	239.82	-0.56218
6	90	FUSx011	1	167.80	314.13	240.96	-0.56056
7	90	FUSx008	1	585.46	644.02	614.74	-0.04591
8	90	uRx016	0	2325.17	1384.42	1854.80	0.08496
9	90	uRx018	0	1916.41	2225.97	2071.19	0.39089
10	90	FUSx014	1	1273.92	1448.23	1361.08	1.01643
11	90	uRx025	0	2935.01	2877.23	2906.12	1.81916
12	90	FUSx009	1	1997.43	1981.08	1989.26	2.27273

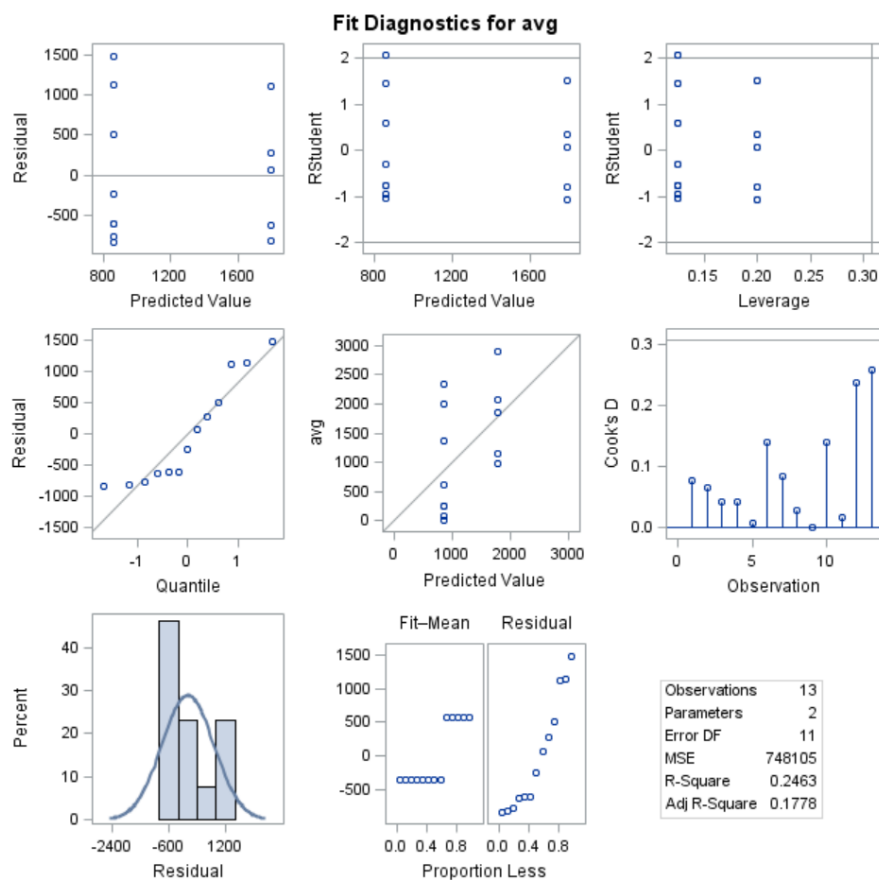
Source	DF	Sum of Squares	Mean Square	F Value	Pr > F
Model	1	2689658.41	2689658.41	3.60	0.0845
Error	11	8229151.84	748104.71		
Corrected Total	12	10918810.25			

R-Square	Coeff Var	Root MSE	avg Mean
0.246333	70.96995	864.9305	1218.728

Source	DF	Type I SS	Mean Square	F Value	Pr > F
trt	1	2689658.407	2689658.407	3.60	0.0845

Source	DF	Type III SS	Mean Square	F Value	Pr > F
trt	1	2689658.407	2689658.407	3.60	0.0845

(a)



(b)

Figure S1: SAS 94 generated figures based on data. (a) P value of 0.0845. (b) The fit diagnostics.

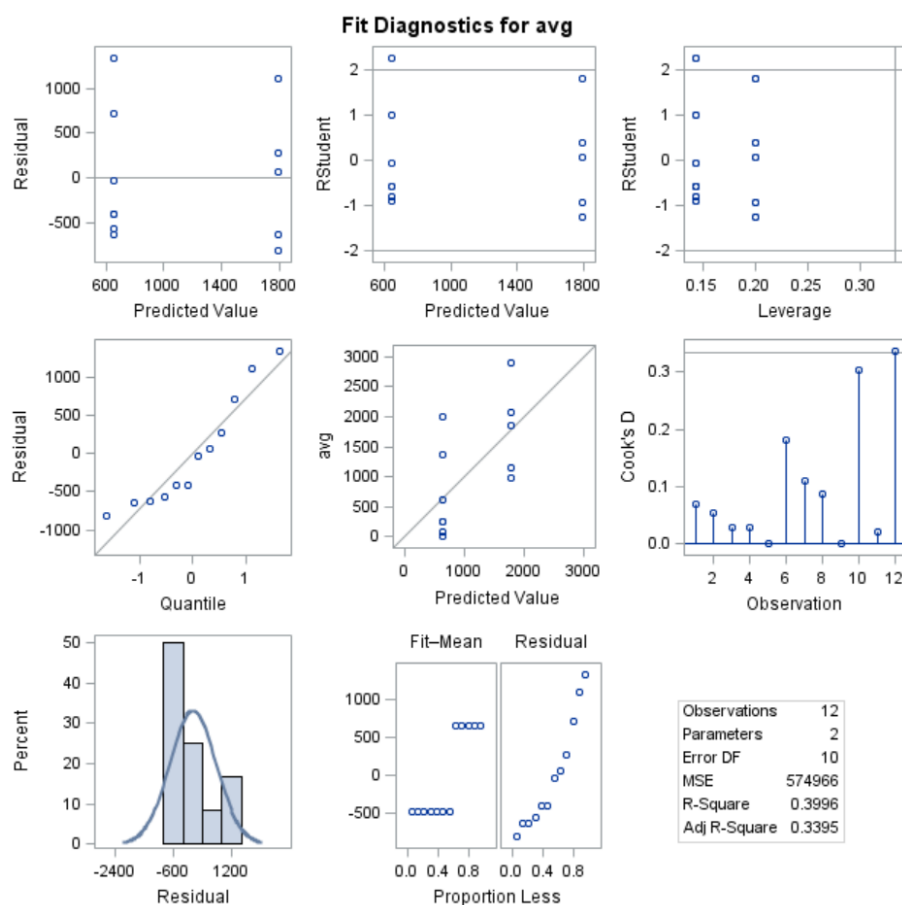
Source	DF	Sum of Squares	Mean Square	F Value	Pr > F
Model	1	3826321.333	3826321.333	6.65	0.0274
Error	10	5749663.560	574966.356		
Corrected Total	11	9575984.893			

R-Square	Coeff Var	Root MSE	avg Mean
0.399575	67.34455	758.2654	1125.949

Source	DF	Type I SS	Mean Square	F Value	Pr > F
trt	1	3826321.333	3826321.333	6.65	0.0274

Source	DF	Type III SS	Mean Square	F Value	Pr > F
trt	1	3826321.333	3826321.333	6.65	0.0274

(a)



(b)

Figure S2: SAS 94 generated figures based on data with removed FUSx005. (a) P value of 0.0274. (b) The fit diagnostics.

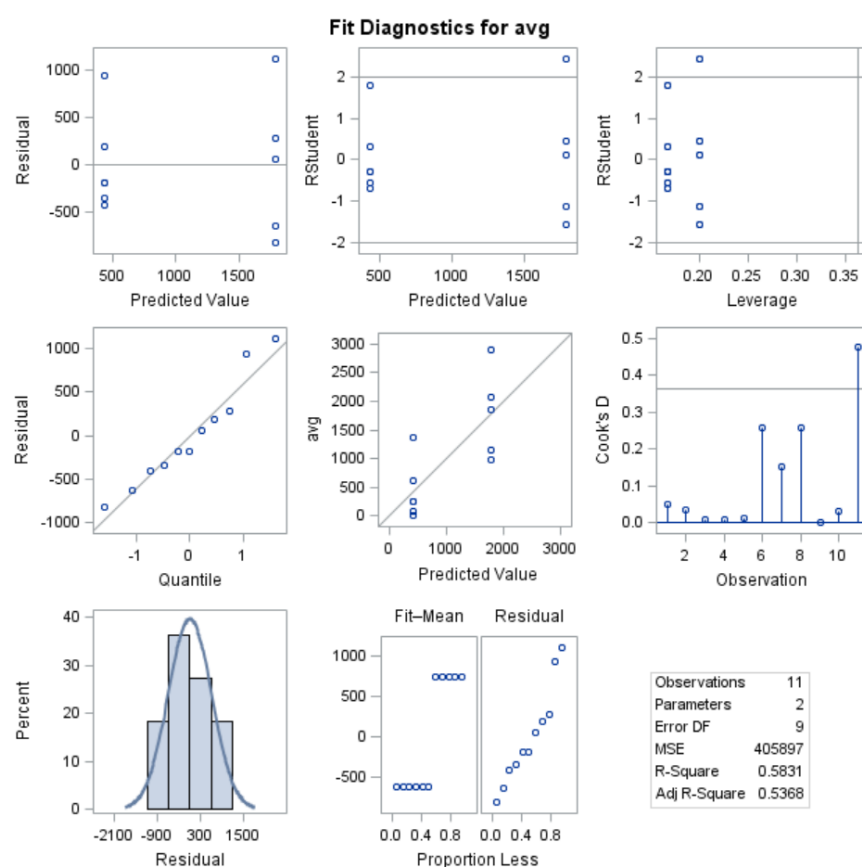
Source	DF	Sum of Squares	Mean Square	F Value	Pr > F
Model	1	5109847.370	5109847.370	12.59	0.0062
Error	9	3653076.874	405897.430		
Corrected Total	10	8762924.244			

R-Square	Coeff Var	Root MSE	avg Mean
0.583121	60.82303	637.1008	1047.466

Source	DF	Type I SS	Mean Square	F Value	Pr > F
trt	1	5109847.370	5109847.370	12.59	0.0062

Source	DF	Type III SS	Mean Square	F Value	Pr > F
trt	1	5109847.370	5109847.370	12.59	0.0062

(a)



(b)

Figure S3: SAS 94 generated figures based on data with removed FUSx005, and FUSx009. (a) P value of 0.0062. (b) The fit diagnostics show a normal distribution and constant variance. These plots support that the assumptions and inferences are valid.

Table S4: Matching Network Components

Value	Size	Rating	Tolerance (%)	Unit Price (\$)
0.1 nF	603	50 V	5%	0.03
1.2 nF	603	50 V	5%	0.14
1.3 nF	603	50 V	5%	0.13
1.5 nF	603	50 V	5%	0.11
1.6 nF	603	50 V	5%	0.27
68 μ H	6.00 x 6.00 x 4.50	1.1 A	20 %	0.47
75 μ H	8.00 x 8.00 x 4.00	1.2 A	20 %	0.90
82 μ H	7.80 x 7.00 x 5.50	1.2 A	10%	0.63

Table S5: Amplification Network Components

Value	Size	Rating	Tolerance (%)	Unit Price (\$)
0.1 μ F	603	50 V	10%	0.19
1.0 μ F	603	50 V	10%	0.11
33 μ H	7.80 x 7.80 x 5.30	1.2 A	10%	0.55
0 Ω	402	N/A	N/A	0.01
Amplifier	4.50 x 4.15 x 1.50	N/A	N/A	1.88
Heatsink forged w/ adhesive tape	19.00 x 19.00 x 12.70	N/A	N/A	5.66

Table S6: Measured V_{pp} values for Prototype I without and with epoxy layer of arbitrary thickness

PZT	V_{pp} (mV)	
	Without Epoxy	With Epoxy
A1	20.50	46.70
A2	5.55	13.06
A3	5.30	10.00
B1	9.32	34.00
B2	5.65	58.00
B3	12.04	17.00
C1	8.47	8.00
C2	9.07	34.00
C3	7.69	8.00

Table S7: Measured impedance values for one PZT element with wires upon arrival, immediately after being incorporated into transducer, and one week after being incorporated into transducer

	Z (ohms)	Theta (degrees)	Shunt (B_L)	Series (X_C)
Arrival	458.60	54.40	114 μ H	1.84 nF
Transducer	676.00	-32.17	62.8 μ H	1.83 nF
Post One Week	633.07	-40.69	61.2 μ H	1.79 nF